

Kinematical Modeling of the Resolved Stellar Outskirts of M32: Constraints on Tidal Stripping Scenarios

IVANNA ESCALA ^{1,2,3} DOUGLAS GRION FILHO ⁴ KAROLINE M. GILBERT ^{1,5} PURAGRA GUHATHAKURTA ⁶
L. R. CULLINANE ^{7,5} MARK FARDAL ⁸ ERIK TOLLERUD ¹ AMANDA C. N. QUIRK ⁹ ZHUO CHEN ¹⁰
MOLLY HYVER,¹¹ AND BENJAMIN F. WILLIAMS ¹⁰

¹*Space Telescope Science Institute, 3700 San Martin Drive, Baltimore, MD 21218, USA*

²*Department of Astrophysical Sciences, Princeton University, 4 Ivy Lane, Princeton, NJ 08544, USA*

³*The Observatories of the Carnegie Institution for Science, 813 Santa Barbara St, Pasadena, CA 91101, USA*

⁴*Department of Astronomy & Astrophysics, University of California Santa Cruz, 1156 High Street, Santa Cruz, CA 95064, USA*

⁵*The William H. Miller III Department of Physics & Astronomy, Bloomberg Center for Physics and Astronomy, Johns Hopkins University, 3400 N. Charles Street, Baltimore, MD 21218, USA*

⁶*UCO/Lick Observatory, Department of Astronomy & Astrophysics, University of California Santa Cruz, 1156 High Street, Santa Cruz, CA 95064, USA*

⁷*Leibniz-Institut für Astrophysik (AIP), An der Sternwarte 16, D-14482 Potsdam, Germany*

⁸*Eureka Scientific*

⁹*Department of Astronomy, Columbia University, 538 West 120th Street, New York, NY 10027, USA*

¹⁰*Department of Astronomy, University of Washington, Box 351580, Seattle, WA 98195, USA*

¹¹*Los Altos High School, 201 Almond Ave, Los Altos, CA 94022, USA*

(Received January 17, 2025; Revised YYY; Accepted ZZZ)

ABSTRACT

As the only compact elliptical close enough to resolve into individual stars, the satellite dwarf galaxy M32 provides a unique opportunity for exploring the origins of such rare galaxies. In this work, we combined archival and novel Keck/DEIMOS spectroscopy from a southern extension of the Spectroscopic and Photometric Landscape of Andromeda’s Stellar Halo (SPLASH) survey with optical HST imaging from the Panchromatic Hubble Andromeda Southern Treasury (PHAST) survey. The resulting sample of 2525 giant stars is unprecedented both in size and spatial coverage (0.9–15.5 arcmin, or out to $\sim 23r_{\text{eff}}$ and $\sim 30r_{\text{eff}}$ along M32’s major and minor axes) for probing the resolved stellar outskirts of M32. Given the structurally complex region near M32 on the sky, we modeled M32’s line-of-sight kinematics simultaneously alongside M31’s rotating stellar disk and potential outliers corresponding to M31’s kinematically hot stellar halo and/or tidal substructure. Inside the radius corresponding to the observed twisting of isophotal contours in M32’s surface brightness profile ($R_{\text{iso}} \sim 5r_{\text{eff}} \sim 150''$ or 0.56 kpc), M32 exhibits a line-of-sight velocity distribution characteristic of ordered rotation, transitioning to a distribution with heavier outliers beyond this radius. Within R_{iso} , the rotational direction is aligned with M32’s major-axis rotation, but shifts to become roughly aligned with M32’s minor axis beyond R_{iso} . We interpret these kinematical signatures in the stellar outskirts of M32 as evidence of tidal distortion from interactions with M31 and discuss their implications for M32 formation pathways.

Keywords: Galaxy formation (595), Dwarf elliptical galaxies (415), Compact dwarf galaxies (281), Stellar kinematics (1608), Andromeda Galaxy (39)

1. INTRODUCTION

The origins of rare compact dwarf elliptical galaxies (cEs), which lie at the relatively low-mass end of the early-type galaxy population ($8 < \log(M_*/M_\odot) < 10$), have long presented a challenge to our understanding of galaxy formation (Mieske et al. 2005; Smith Castelli

et al. 2008; Chilingarian et al. 2007, 2009; Price et al. 2009; Norris et al. 2014; Chilingarian & Zolotukhin 2015; Ferré-Mateu et al. 2018, 2021; Caso et al. 2024). With only approximately 200 known cEs in the local universe, these galaxies typically have effective radii between 0.1–0.7 kpc, which is smaller than their low-density dwarf elliptical counterparts at a given stellar mass. Although cEs appear to follow some typical galaxy scaling relations (Kormendy et al. 2009; Paudel et al. 2014), they tend to be significant outliers on the stellar mass–metallicity relation for early-type galaxies (e.g., Gallazzi et al. 2005; Kirby et al. 2013).

Moreover, cEs have been found in a variety of environments (e.g., Norris et al. 2014), ranging from those clearly interacting with a massive host galaxy (Huxor et al. 2011) to those that appear to be isolated (Huxor et al. 2013; Paudel et al. 2014). Metal-rich cEs near a host may be the remnants of tidally stripped massive progenitors (Bekki et al. 2001; Khoperskov et al. 2023, but see also Du et al. 2019; Bian et al. 2024), whereas isolated cEs could either have been ejected from their original galactic systems by gravitational interactions (Chilingarian & Zolotukhin 2015) or have formed in an intrinsically compact state (Burkert 1994; Kormendy et al. 2009). Recent observational studies support a mix of formation pathways for cEs (e.g., Ferré-Mateu et al. 2018, 2021), although their relative contributions still warrant exploration in a cosmological context (Deeley et al. 2023; Jang et al. 2024; Bian et al. 2024).

The nearby compact dwarf elliptical satellite galaxy, M32, is the prototype for the cE class. As the only cE close enough to resolve into individual stars, M32 provides a unique opportunity for exploring cE origins. Even among cEs, M32 has extreme properties: it is highly compact ($r_{\text{eff}} \sim 0.1$ kpc; Choi et al. 2002) and a significant outlier on the stellar mass–metallicity relation ($[\text{Fe}/\text{H}] \sim -0.2$; Monachesi et al. 2011). The stellar mass and dynamical mass within r_{eff} of M32 is approximately $M_{\star} \sim 3.2 \times 10^8 M_{\odot}$ and $5.2 \times 10^8 M_{\odot}$ respectively (Bender et al. 1996; McConnachie 2012), where M32 is known to possess a central supermassive black hole ($M_{\text{BH}} \sim 2 - 4 \times 10^6 M_{\odot}$; Joseph et al. 2001; van der Marel et al. 1997; Verolme et al. 2002; van den Bosch & de Zeeuw 2010). Integrated light studies suggest the presence of a central population of young metal-rich stars in M32 (Schiaffon et al. 2004; Rose et al. 2005; Coelho et al. 2009), where resolved stellar photometry also shows evidence for a substantial intermediate-age population (Monachesi et al. 2011, 2012; Jones et al. 2023).

Owing to its proximity to M31 ($D_{\text{M31}} = 20.6_{-21}^{+13}$ kpc; Savino et al. 2022), tidal interactions may provide a

plausible formation pathway for M32 that could explain its unusual properties. M32 could be the remnant bulge of a spiral galaxy that was tidally stripped inside M31’s potential (Bekki et al. 2001), or alternatively, M32 may have originally been a dwarf galaxy that was compacted over a series of interactions with M31, but without experiencing significant mass loss (Du et al. 2019). In particular, the former hypothesis has long been an explanation for M32’s origin based on its compact nature and its metal-rich intermediate-age stellar populations.

Upon discovery of M31’s Giant Stellar Stream (GSS), Ibata et al. 2001 proposed M32 as a possible candidate for the stream’s progenitor owing its clear status as a bright and close companion of M31. Williams et al. 2015 further speculated that M32 may be the remnant of a massive, gas-rich galaxy that strongly interacted with M31 2–4 Gyr ago, triggering similarly timed starbursts both in M31’s disk and M32 (Monachesi et al. 2012; Bernard et al. 2015). More recently, D’Souza & Bell 2018 argued that M32 may be the core of an M33- or LMC-mass spiral galaxy based on the observed properties of M31’s massive, metal-rich, and intermediate-age stellar halo, which point to a single dominant merger when compared to cosmological simulations. This scenario could simultaneously explain M31’s system of major tidal features, which includes the GSS, and the observed properties of both M31’s disk and M32.

Numerical simulations of the evolution of M31-like systems have provided potential clues about the origins of M32. Early N-body simulations of interactions between spherical or elliptical progenitors and an M31-like host (Choi et al. 2002; Johnston et al. 2002) concluded that M32 was unlikely to have experienced significant tidal evolution (e.g., Peñarrubia et al. 2008), but could not rule out the bulge of a spiral galaxy as its precursor. Subsequent modeling tailored to the M31-M32 interaction focused on scenarios involving recent ($\lesssim 800$ Myr) off-center collisions between M32 and M31’s disk in an attempt to reproduce M31’s star-forming rings, including the split in the 10 kpc ring near M32 on the sky (Gordon et al. 2006; Block et al. 2006; Dierickx et al. 2014). However, the long-term stability of the 10 kpc star-forming ring on $\gtrsim 500$ Myr timescales (Lewis et al. 2015) largely rules out a recent collision between M32 and M31’s disk in the context of existing models, at least as an explanation for M31’s young stellar and gaseous features (c.f. Davidge et al. 2012). For example, simulations of a major merger in an M31-like system with an $M_{\star} \sim 10^{10} M_{\odot}$ progenitor occurring 2–3 Gyr ago can reproduce M31’s star-forming ring without invoking an M32-like galaxy (Hammer et al. 2010, 2018). Moreover, the first and only self-consistent model of the M31-M32

interaction found tidal stripping of an initially massive M32 ($M_{\text{tot}} \sim 10^{10} M_{\odot}$) over a single pericentric passage to be insufficient in terms of producing a compact elliptical morphology, thereby concluding that cEs like M32 may be intrinsically compact (Dierickx et al. 2014).

Existing observational measurements suggest minimal direct evidence for tidal stripping within M32’s central ~ 1 kpc, at face value supporting an intrinsically compact origin. Despite the presence of elongated isophotes in M32’s outer surface brightness profile, Choi et al. 2002, hereafter C02, estimated that M32’s effective radius experienced little evolution with time and therefore was not influenced by tidal distortions. However, Graham 2002 argued that the surface brightness profile over the full radial range probed was better explained by a Sérsic bulge and “fossil” exponential disk, which corresponds to M32’s observed excess light at large radii, than the elliptical de Vaucouleurs profile of C02. The only resolved stellar kinematical study of M32’s outskirts to date (Howley et al. 2013, hereafter H13) found little evidence of tidal distortion within $\sim 8r_{\text{eff}}$, with no detected change in kinematics across the region where M32’s isophotal elongation begins (C02). In addition, there is no clear observational connection between M32 and tidal debris in M31’s stellar halo that may correspond to stripped material from M32’s putative progenitor, where M32’s present-day position is inconsistent with current predictions from N-body models for the location of the GSS progenitor core on the eastern side of M31 (Fardal et al. 2013; Escala et al. 2022).

In this work, we revisit M32’s resolved stellar kinematics with the goal of placing updated observational constraints on M32’s velocity structure at large radii to inform its origins as a cE galaxy, particularly scenarios involving strong tidal interactions with M31. Resolved kinematical studies of M32 are lacking owing to M32’s steep surface brightness profile combined with its projected location at the edge of M31’s disk, such that observations must contend with both stellar crowding and contamination from M31. To circumvent this, we utilize an expanded dataset in sample size and areal coverage, combining all available ground-based Keck/DEIMOS stellar spectroscopy in the vicinity of M32 from southern extensions of the Spectroscopic and Photometric Landscape of Andromeda’s Stellar Halo survey (SPLASH; e.g., Guhathakurta et al. 2005; Gilbert et al. 2006, 2012; Tollerud et al. 2012) with high-precision Hubble Space Telescope (HST) photometry from the Panchromatic Hubble Andromeda Southern Treasury (PHAST; Chen et al. 2025, accepted). PHAST is a new legacy survey imaging the southern half of M31’s star-forming disk at optical and near-ultraviolet wavelengths, covering key

diagnostic features sensitive to M31’s complex merger history, specifically including intersections with M32.

We summarize the observations and construction of the full spectroscopic dataset in Section 2 and identify giant stars in M32 and M31 from the sample in Section 3. In Section 4, we apply a spatially continuous Bayesian mixture model to describe the line-of-sight velocity distribution of the structurally complex region near M32 to isolate the kinematics of the dwarf galaxy relative to stellar populations in M31. We present M32’s velocity structure with respect to its “inner” and “outer” regions as defined by its surface brightness profile in Section 5 and discuss implications for M32’s origin in Section 6. Throughout this work, we assume that M32 and M31 are located at the same distance ($D_{\text{M31}} = 776.2_{-21}^{+22}$ kpc; Savino et al. 2022).

2. SPECTROSCOPIC DATA

We combined previously unpublished and archival resolved stellar spectroscopy obtained with the DEIMOS instrument on Keck II to produce a sample of 2712 stars with successful velocity measurements unprecedented both in size and spatial coverage of the stellar outskirts of M32. Table 1 summarizes each observational program and Figure 1 shows the approximate footprint of the combined set of 20 DEIMOS slitmasks, in addition to targets with successfully extracted 1D spectra for each program. In Sections 2.1 and 2.2, we describe the program-specific observational details for unpublished spectroscopy from campaigns in Fall 2022 (Grion Filho et al., in preparation) and Fall 2019 (Fardal et al., in preparation) respectively. Section 2.3 outlines the spectroscopy from Fall 2007 and 2008 published by H13. When constructing the combined spectroscopic sample of unique targets, we flagged duplicates present across each individual sample, giving preference to the 2022B, 2019B, and H13 samples in that order.

For all observations, the 1200 ℓ/mm DEIMOS grating was used with the OG550 order blocking filter and a central wavelength of 7800 \AA for the science configuration, resulting in a spectral dispersion of 0.33 \AA per pixel, with ~ 1 hr science exposures. The two-dimensional and one-dimensional spectra were reduced using versions of the `spec2d` and `spec1d` pipelines (Cooper et al. 2012; Newman et al. 2013) modified for stellar sources (Simon & Geha 2007). Radial velocities were obtained by cross-correlating the one-dimensional spectra against empirical templates of hot stars, including A-band corrections for slit miscentering (Sohn et al. 2007) and heliocentric corrections. The total velocity uncertainty was determined by scaling the cross-correlation based error with a value determined from duplicate measurements of RGB

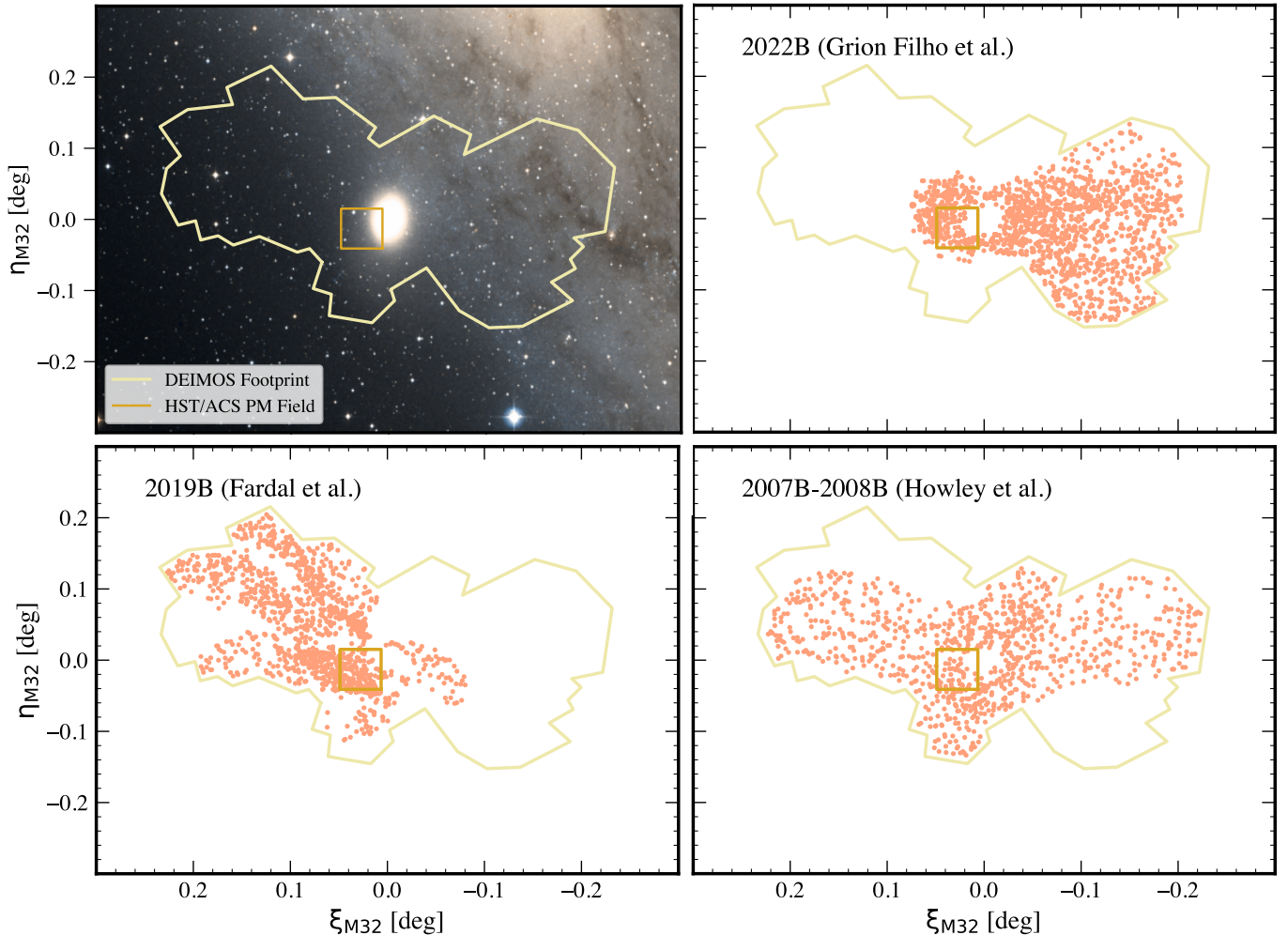


Figure 1. (Upper left) Approximate footprint of Keck/DEIMOS spectroscopic fields (yellow outline) in the vicinity of M32 used in this work (Section 2; Table 1), overlaid on a DSS image of M32 and M31. We also show the location of an archival HST/ACS field targeting M32 (orange rectangle; HST GO 9392 and 15658) suitable for proper motion measurements (Fardal et al., in preparation; Patel et al., in preparation). (Upper right and bottom panels) Sky location of spectroscopic targets with successfully extracted 1D spectra (excluding serendipitous detections), separated according to observing program (2022B, 2019B, H13). The central regions are inaccessible for ground-based resolved stellar spectroscopy due to crowding.

stars at the distance of M31 (H13), and then adding in quadrature with a systematic velocity error of 2.2 km s^{-1} computed by Simon & Geha (2007).

To assess the reliability of the velocity measurements, the raw two-dimensional spectra, extracted one-dimensional spectra, and best-fit empirical templates were visually inspected in the `zspec` software (D. Madgwick, DEEP2 survey) and assigned a quality code (Q ; e.g., Guhathakurta et al. 2006). We restrict our analysis to objects with successful radial velocity measurements, which match at least one strong spectral feature ($Q = 3$ or $Q = 4$). The median total velocity uncertainty across the entire sample is 4.2 km s^{-1} given a median sample signal-to-noise ratio (S/N) of 5.1 per pixel.

2.1. 2022B (Grion Filho et al.) Observations

We observed nine slitmasks targeting M32 in a “Japanese fan” pattern with Keck/DEIMOS in Fall 2022 as part of a spectroscopic survey of M31’s southwestern disk region (Grion Filho et al., in preparation).¹ This survey is designed as a complement to the Spectroscopic and Photometric Landscape of Andromeda’s Stellar Halo survey of M31’s northeastern disk region (SPLASH; Dorman et al. 2012, 2013, 2015), which selected targets in part from the HST-based Panchromatic

¹ We observed a tenth mask, M32RA2, which is excluded from this analysis owing to significant issues with the wavelength solution. It will be included in a forthcoming paper (Grion Filho et al., in preparation).

Table 1. Summary of Keck/DEIMOS Observations in the Vicinity of M32

Slitmask	R.A.	Decl.	Mask P.A. (° E of N)	Obs. Date (UT)	t_{exp} (min)	Airmass	No. Targets ^a	No. RV ^b
2022B (Grion Filho et al.)								
M32RA1	00:42:25.56	+40:54:20.3	-186.2	2022 Sep 27	60.0	1.07	175	173
M32RB1	00:42:19.34	+40:54:13.8	-237.4	2022 Sep 28	60.0	1.18	175	169
M32RB2	00:42:19.57	+40:54:08.6	-226.0	2022 Sep 27	60.0	1.13	166	157
M32RC1	00:42:20.52	+40:52:39.8	-99.4	2022 Sep 27	60.0	1.52	184	177
M32RC2	00:42:21.09	+40:52:38.9	+111.6	2022 Sep 27	76.8	1.28	176	156
M32RD1	00:42:23.35	+40:51:18.2	-116.0	2022 Sep 27	60.0	1.23	177	171
M32RD2	00:42:23.76	+40:51:18.4	-111.4	2022 Sep 28	60.0	1.28	172	160
M32RE1	00:42:21.55	+40:49:40.8	-133.4	2022 Sep 28	54.0	1.13	185	183
M32RE2	00:42:21.15	+40:49:38.6	-143.8	2022 Sep 27	60.0	1.10	179	174
2019B (Fardal et al.)								
m32p2a	00:43:03.14	+40:56:28.6	-177.0	2019 Oct 23	67.3	1.07	214	103
m32p2b	00:43:02.86	+40:56:30.6	-115.8	2019 Oct 23	95.0	1.23	212	111
m32p3a	00:43:18.52	+40:54:38.2	-110.4	2019 Oct 22	95.0	1.29	216	90
m32p3b	00:43:18.66	+40:54:35.3	-89.6	2019 Oct 22	88.3	1.96	213	107
m32pm1	00:43:00.21	+40:53:28.4	-158.2	2019 Oct 22	85.1	1.08	223	126
m32pm4	00:43:00.29	+40:50:23.8	-94.0	2019 Oct 23	80.0	1.71	210	111
2007B–2008B (Howley et al.)								
M32_1	00:42:38.55	+40:51:29.7	-112.6	2007 Nov 14	60.0	1.26	201	187
M32_2	00:43:04.03	+40:55:07.1	-95.6	2008 Aug 03	60.0	1.64	192	167
M32_3	00:43:11.34	+40:52:41.7	-110.7	2008 Aug 03	60.0	1.29	199	134
M32_4	00:42:14.59	+40:54:39.0	-121.8	2008 Aug 04	60.0	1.18	152	134
M32_5	00:42:14.50	+40:52:11.4	-152.7	2008 Aug 04	60.0	1.09	183	157

^a Number of targets on the slitmask with successfully extracted one-dimensional spectra, excluding serendipitous detections.

^b Number of targets with successful radial velocity measurements (Section 2).

Hubble Andromeda Treasury (PHAT) survey (Dalcanton et al. 2012; Williams et al. 2014).

Figure 1 shows the location of spectroscopic targets on the 2022B masks in M32-centric coordinates. The fan pattern, which is anchored to the east of M32’s compact center, was designed to increase the density of spectroscopic targets near M32’s center while simultaneously including repeat targets on overlapping masks. The primary purpose of the repeat targets is to enhance the S/N for spectra of individual stars with higher probabilities of being associated with M32 (>40%) in order to measure their detailed chemical abundances in future work (Escala et al., in preparation).²

We identified probable M32 stars by computing a likelihood based on the relative I-band surface brightness between M32 and M31 ($p_{\text{M32,SB}}$). Following H13, we modeled the 2D surface brightness of M32 as a series of isophotes with varying I-band surface brightness, ellipticity and position angle as a function of major/minor

axis distance from M32 (C02; Figure 2). We modeled the 2D surface brightness profile of M31 as the sum of a Sérsic bulge, exponential disk, and cored power-law halo as a function of M31-centric projected radius and position angle, assuming the structural parameters derived by Dorman et al. 2013 from combining PHAT luminosity functions with SPLASH radial velocities (see their Table 2 and Section 4.1.1). The M32 probability for a given star is thus the ratio of the predicted M32 versus M31 I-band magnitudes at its location, $p_{\text{M32,SB}} = I_{\text{M32}} / (I_{\text{M31}} + I_{\text{M32}})$, where $I_{\text{M32}} = 10^{-2\Sigma_{\text{M32}}/5}$ and $\Sigma_{\text{M32}}(\alpha, \delta)$ is the 2D surface brightness in magnitudes per square arcsecond at sky coordinates (α, δ) . On average, we expect M31’s bulge, disk, and halo components to contribute 2.5%, 92.6%, and 4.9% respectively

² When constructing our final sample of unique targets, we selected the observation with the highest S/N spectrum per repeat target.

to M31’s total light over the DEIMOS footprint near M32 (Figure 1).³

When designing the 2022B observations, we selected isolated targets from stellar catalogs based on HST/ACS photometry from PHAST (Chen et al. 2025, accepted). We identified crowded sources in the PHAST catalog using the empirical isolation criterion of H13, which excludes a given star as a possible spectroscopic target if the point spread function (PSF) of any of its neighbors significantly overlaps with that of the target,

$$m_{\text{tgt}} > m_{\text{nbr}} + \frac{\theta_{\text{tgt,nbr}}}{\theta_{\text{DEIMOS}}} - m_{\text{lim}}, \quad (1)$$

where m_{tgt} and m_{nbr} are the F814W magnitudes of a given target and neighbor, $\theta_{\text{tgt,nbr}}$ is the angular separation on the sky between the target and neighbor, $\theta_{\text{DEIMOS}} = 0.8''$ is the typical seeing at Keck II, and $m_{\text{lim}} = 3$ corresponds to the faintest magnitude difference for which a neighbor star may significantly contaminate the PSF of the target star. Based on this criterion, M32’s central $\sim 1'$ ($\mu_I \sim 18.9$ mag arcsec⁻²) is sufficiently crowded that PHAST giant star candidates are inaccessible for ground-based spectroscopy (Figure 1).

Slitmasks designated “1” primarily target red giant branch (RGB) star candidates, whereas slitmasks designated “2” primarily target asymptotic giant branch (AGB) and red-helium burning (RHeB) star candidates at approximately the same mask placement (Table 1).⁴ We identified RGB, AGB, and RHeB candidates based on (F475W, F814W) selection boxes in the PHAST color-magnitude diagram (CMD; Figure 3).⁵ We targeted stars of different spectral types and therefore different mean stellar ages in order to perform age-dependent kinematical analyses in M31’s southern disk region in future work (c.f. Dorman et al. 2015; Quirk et al. 2019; Grion Filho et al., in preparation). We also

³ As discussed in Section 5, M31’s global surface brightness profile is known to substantially overpredict M31’s disk fraction relative to M31’s spheroid in the vicinity of M32 (see Appendix by Dorman et al. 2012 and discussion by H13). Throughout this work, we utilize $p_{\text{M32,SB}}$ only as guide on where to expect M32 stars based on the surface brightness profile alone.

⁴ RGB candidates that had higher surface-brightness based a priori probabilities of belonging to M32 were given higher priority as targets (for chemical abundance measurements), whereas no distinction was made among RHeB or AGB candidates based on their likelihood of being associated with M32.

⁵ These selection boxes, which were used only for spectroscopic target selection in the 2022B slitmask design, differ from the RGB and AGB classification criteria homogeneously adopted across all observational samples (Figure 3; Section 3.2). Moreover, stars classified as RHeB in the 2022B mask design tend to be conservatively assigned as belonging to the MW foreground based on photometry alone in our membership determination (Section 3.1).

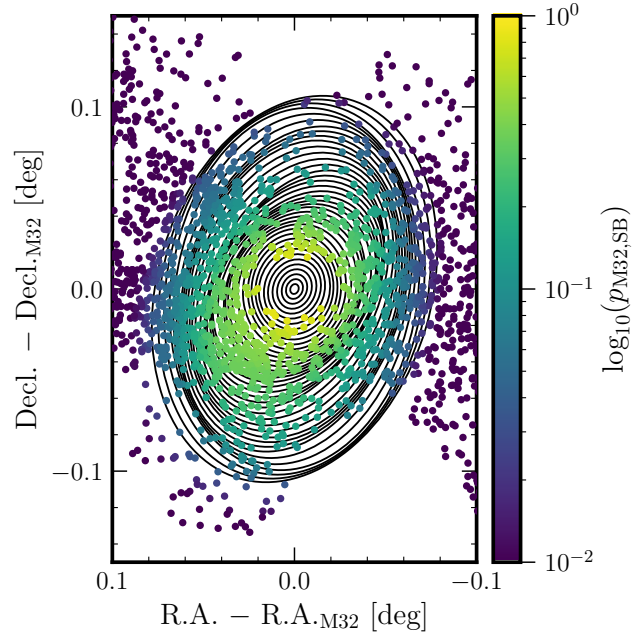


Figure 2. Location of spectroscopic targets near M32 (Table 1; Section 2), colored by the probability of belonging to M32 based on the relative I-band surface brightness between M32 (C02) and M31 (assuming a bulge, disk, and halo model; Dorman et al. 2013). We also show M32 isophotes from C02 for reference (black curves). Owing to M32’s steep surface brightness profile and contamination from M31’s disk to the northwest (Figure 1), the likelihood that a given target belongs to M32 decreases rapidly with projected radius from M32’s center.

placed 28 planetary nebulae (PNe) as spectroscopic targets on the slitmasks (Bhattacharya et al., in preparation), which we exclude from this analysis.

2.2. 2019B (Fardal et al.) Observations

In Fall 2019, Fardal et al., in preparation observed six slitmasks targeting an HST/ACS field (HST GO 9392 and 15658) suitable for proper motion measurements near M32’s core to obtain complementary line-of-sight velocity measurements for individual stars from spectroscopy. Figure 1 shows a dense clustering of targets at the location of the HST field. For this observing program, the position angle of the slitmasks increases with mask index (1–4; Table 1), where masks labeled “a” and “b” in each pair share the same spatial position and orientation while targeting different stars.

Photometric catalogs for HST fields were obtained from the Hubble Legacy Archive (HLA). Spectroscopic targets were selected from a combination of archival HST-based ACS F814W-band (GO 9392, PI Mateo; Rudenko et al. 2009; GO 10273, PI Crofts; Csereny et al. 2005; GO 13691, PI Freedman; Beaton et al. 2016), WFPC2 F814W-band photometry (GO

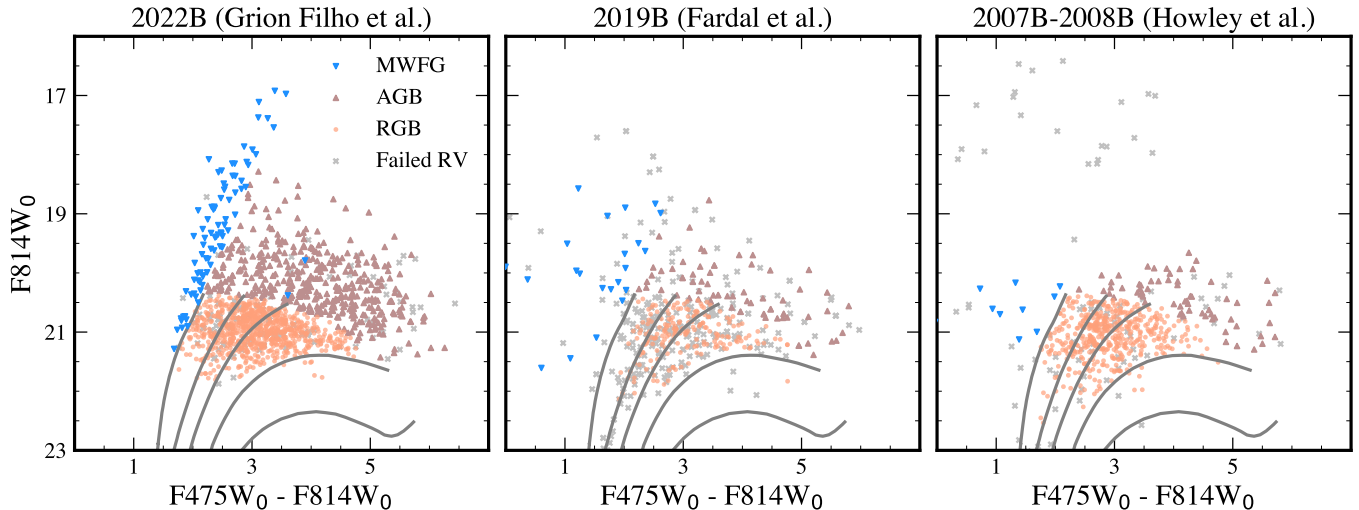


Figure 3. Extinction-corrected ($F475W_0$, $F814W_0$) PHAST (Chen et al. 2025, accepted) CMD for all stars with original and matched photometry separated according to observational sample (Section 2; Table 1). We show stars without successful velocity measurements (gray crosses), stars assigned to the MW foreground (which includes RHeB stars in M31 excluded from our sample; blue inverted triangles), and RGB (orange circles) and AGB (brown triangles) stars assigned to M31 or M32 (Section 3). The median photometric errors are $\delta m_{F475W} = 0.03$ and $\delta m_{F814W} = 0.006$. For reference, we show PARSEC isochrones (gray lines; Bressan et al. 2012; Tang et al. 2014; Chen et al. 2015) assuming 12 Gyr ages and $[\alpha/\text{Fe}] = 0$ with $[\text{Fe}/\text{H}] = -2.0, -1.0, -0.5, \text{ and } 0$ (from left to right).

8059, PI Casertano), ACS F606W-band photometry (GO 10572, PI Lauer; Sarajedini et al. 2009; Monachesi et al. 2011), and ACS F775W-band photometry (GO 9480, PI Rhodes), as well as CFHT/MegaCam i -band photometry from the Pan-Andromeda Archaeological Survey (PAndAS; McConnachie et al. 2009, 2018).

Fardal et al. used linear transformations to place the astrometry for all photometric sources on the *Gaia* DR2 reference frame. The final list of possible spectroscopic targets was limited to relatively uncrowded stars using a similar isolation criterion to Eq. 1 (Dorman et al. 2012) and stars with magnitudes $-3 \lesssim m_{\text{TRGB}} - m \lesssim +1.5$ (defined in the F814W band or similar). Targets selected from HST photometry were prioritized over those selected from the ground-based PAndAS survey owing to the higher likelihood of blending in the CFHT images.

Given that the available photometry is limited to a single band per source program and that a mix of filters was used for selecting spectroscopic targets, we matched targets with successfully extracted 1D spectra to ($F475W$, $F814W$) photometry from PHAST. We restricted potential matches to stars in the PHAST catalog meeting the “good star” criteria from Williams et al. 2021 based on DOLPHOT (Dolphin 2000, 2016) quality flags in each band. For each spectroscopic target, we searched for matches within a $0.5''$ radius. If F814W photometry was unavailable for a given spectroscopic target, we selected the PHAST target with the brightest F814W magnitude as the match. Alternately, if F814W

photometry was available, we required that the magnitude of the match agreed with that of the spectroscopic target within 2σ of the PHAST photometric errors. Figure 3 shows the CMD for all stars with matched PHAST photometry in the 2019B sample.

2.3. 2007B–2008B (Howley et al.) Observations

We used archival Keck/DEIMOS spectroscopy of five slitmasks targeting M32 published by H13. Figure 1 shows the H13 targets with successfully extracted 1D spectra, where a single slitmask is oriented along M32’s major axis (P.A. ~ -22 deg E of N) and the remaining slitmasks are positioned to optimize coverage of M32’s outer regions where isophotal distortion is present ($R_{\text{M32}} > 150'' \sim 5r_{\text{eff}}$; C02; Figure 2), in addition to M31’s disk and halo (Dorman et al. 2012).

H13 selected spectroscopic targets from archival single-band CFHT/MegaCam i' photometry (obtained at $0.8''$ seeing) in the magnitude range $i' = 20 - 21.5$. They rejected targets that were affected by crowding (Eq. 1) or blending, where the latter effect was assessed based on visual inspection of the PSF in the MegaCam images. Given that the seeing ($0.6''$) during spectroscopic observations exceeded that of the photometry used in the mask design, H13 performed further deblending in the spatial and spectral domains by identifying serendipitously detected sources.

Similar to the case of the 2019B observations (Section 2.2), we matched the H13 targets to stars in the

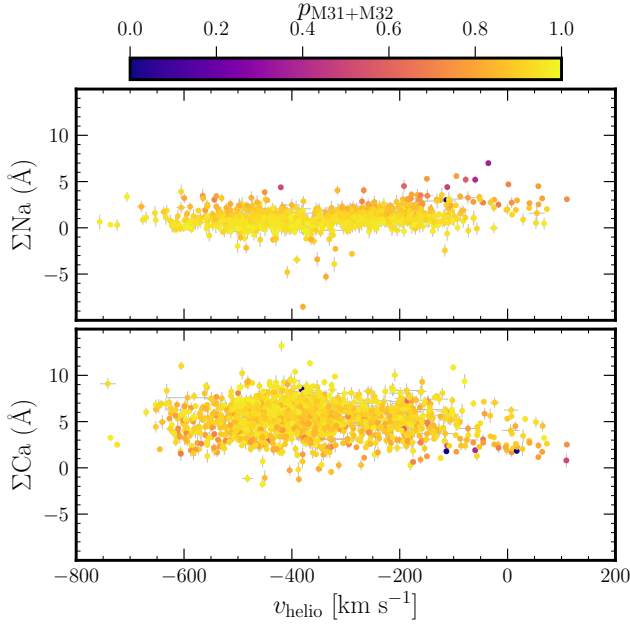


Figure 4. (Left) Summed equivalent width of the Na I $\lambda 8190$ doublet (ΣNa) and (right) summed equivalent width of the Ca II triplet near $\lambda 8500$ (ΣCa) following Rutledge et al. (1997) versus heliocentric velocity (v_{helio}). We show all stars with successful velocity measurements and equivalent width measurements with $\delta\Sigma\text{Na} < 0.8 \text{ \AA}$ or $\delta\Sigma\text{Ca} < 0.8 \text{ \AA}$ for clarity (Section 3.1). Each star is color-coded by the probability that it belongs to M31 or M32 versus the MW foreground ($p_{\text{M31+M32}}$) based on population diagnostics (ΣEW , ΣCa , and CMD position; Escala et al. 2020b). Most stars have a high probability of being associated with M31 or M32.

PHAST stellar catalog based solely on their spatial position, adopting the (F475W, F814W) photometry of the brightest star within the $0''.5$ search radius. Figure 3 shows the PHAST CMD for all targets with matched photometry, where a number of bright targets ($m_{\text{F814W}} < 19$) with failed radial velocity measurements likely reflects the presence of crowded/blended sources selected as spectroscopic targets owing to the limitations of the MegaCam imaging.

3. M31 & M32 MEMBERSHIP DETERMINATION

In this section, we evaluate the spectroscopic and photometric properties of the stellar sample from Section 2 to associate stars with M31 or M32 (as opposed to the MW foreground; Section 3.1). We also separate the sample into populations based on stellar type (Section 3.2).

3.1. Identifying M31/M32 Giant Stars

We assigned stars to the MW foreground based on the equivalent width of the surface-gravity sensitive Na I $\lambda 8190 \text{ \AA}$ doublet (ΣNa), the strength of the metallicity-

sensitive Ca II triplet absorption feature near 8500 \AA (ΣCa), and PHAST CMD position. We used these diagnostics in the context of the model developed by Escala et al. 2020b, which relies on Bayesian inference to assign each target star a probability of M31 versus MW membership based on the observed properties of over a thousand M31 and MW stars securely identified as part of the SPLASH survey of M31’s southeastern stellar halo (Gilbert et al. 2006, 2012). Although intended for M31 halo stars, the model is useful for identifying RGB and AGB stars in M32 (and in M31’s disk, which should be the dominant M31 stellar population in our dataset; Section 2.1) because M32 giant stars have low surface gravity, high metallicity, and red CMD positions similar to M31 giants and relative to the MW foreground.

In contrast to Escala et al. (2020b), we do not use radial velocity (v_{helio}) as a membership diagnostic to avoid kinematically biasing our analysis, where stars with MW-like velocities ($v_{\text{helio}} \gtrsim -150 \text{ km s}^{-1}$; Gilbert et al. 2012) significantly overlap with the expected velocity distribution of M32 ($\mu_v \sim -200 \text{ km s}^{-1}$, $\sigma_v \sim 30 \text{ km s}^{-1}$; Dorman et al. 2012; Howley et al. 2013). In addition, we modified the Bayesian membership model to use ΣCa as a diagnostic instead of the calcium-triplet based spectroscopic metallicity ($[\text{Fe}/\text{H}]_{\text{CaT}}$), which relies on a calibration between ΣCa , Johnson-Cousins V/I magnitude, and metallicity. Following Rutledge et al. 1997,

$$\Sigma\text{Ca} = 0.5 \times \text{EW}_{\lambda 8498} + 1.0 \times \text{EW}_{\lambda 8542} + 0.6 \times \text{EW}_{\lambda 8662}, \quad (2)$$

where EW is the equivalent width of an absorption feature at a given wavelength. Due to the dependence of $[\text{Fe}/\text{H}]_{\text{CaT}}$ on ΣCa , the latter diagnostic similarly demonstrates a clear difference in the distributions corresponding to secure M31 (MW) stars in SPLASH: $\langle \Sigma\text{Ca} \rangle = 5.60$ (3.00) \AA and $\langle \delta\Sigma\text{Ca} \rangle = 1.71$ (0.88) \AA . The advantages of using ΣCa instead of $[\text{Fe}/\text{H}]_{\text{CaT}}$ are twofold given that $[\text{Fe}/\text{H}]_{\text{CaT}}$ calibrations depend on apparent magnitude: the reliance on transformations between the ACS and Johnson-Cousins photometric systems (e.g. Sirianni et al. 2005) is eliminated and information from ΣCa remains usable even in the absence of PHAST-matched photometry (Section 2.2, 2.3).

We parameterized CMD position by converting extinction-corrected PHAST colors and magnitudes into a metric (X_{CMD} ; Escala et al. 2020b) that is measured relative to 12 Gyr (F475W, F814W) PARSEC isochrones (Bressan et al. 2012; Tang et al. 2014; Chen et al. 2015). We corrected for the effects of dust extinction caused by the MW foreground by assuming the median value over the low extinction PAndAS footprint ($A_{V,\text{MW}} = 0.2$; McConnachie et al. 2018) based on the dust maps by Schlegel et al. (1998) with modifications

by Schlafly & Finkbeiner (2011), or $A_{F814W} = 0.12$ and $A_{F475W} = 0.38$ when transformed to the appropriate ACS filters (Gregersen et al. 2015).

Based on homogeneous RR Lyrae-based distances, M32 and M31 are consistent with being located at the same distance ($\mu_{M32} \sim 24.44 \pm 0.06$, or $D_{M31} = 20.6^{+13}_{-21}$; Savino et al. 2022), implying that M32 observations are not significantly impacted by dust in M31. Moreover, M32 shows a lack of internal interstellar dust reservoirs (e.g., Choi et al. 2002; Fiorentino et al. 2010; Sarajedini et al. 2012). M31 disk stars present in our dataset may be subject to internal dust extinction (Draine et al. 2014; Dalcanton et al. 2015), although the stellar properties of RGB stars observed by the SPLASH survey of M31’s northeastern disk show little evidence of being affected by internal reddening (Escala et al. 2023).

This parametrization provides a filter-independent means of comparison against the CMD positions of M31/MW SPLASH stars. We conservatively assigned stars with HST colors bluer than the most metal-poor PARSEC isochrone ($[\text{Fe}/\text{H}] = -2.2$) by an amount greater than the photometric uncertainty to the MW foreground (Gilbert et al. 2006; Escala et al. 2020b). Figure 3 shows that this criterion excludes RHeB candidates intentionally placed on the 2022B slitmasks ($16.6 \lesssim m_{F814W} \lesssim 20.6$, $2 \lesssim (m_{F475W} - m_{F814W}) \lesssim 3$) that likely correspond to young M31/M32 giant stars with colder kinematics (Dorman et al. 2015; Quirk et al. 2019, 2022; Grion Filho et al., in preparation). However, as we demonstrate below, the details of the membership determination have little impact on the structure of the resulting velocity distribution.

For some stars in our sample, we were unable to measure ΣNa and/or ΣCa due to weak absorption, low spectral S/N, or convergence failure in the Gaussian fit of the absorption features (Escala et al. 2020b). Moreover, some stars lack matched PHAST photometry, such that their CMD position could not be used as a diagnostic. In these instances, we used all diagnostic information available to compute a probability of M31/M32 membership, as long as a given star has a successful measurement of ΣNa , ΣCa , or PHAST photometry. We excluded 66 stars with no available diagnostic measurements from the total sample of 2712 stars with successful velocity measurements from the subsequent analysis.

Figure 4 shows the relationship between heliocentric velocity (v_{helio}) and ΣNa or ΣCa , color-coded by the probability that it belongs to M31 or M32 versus the

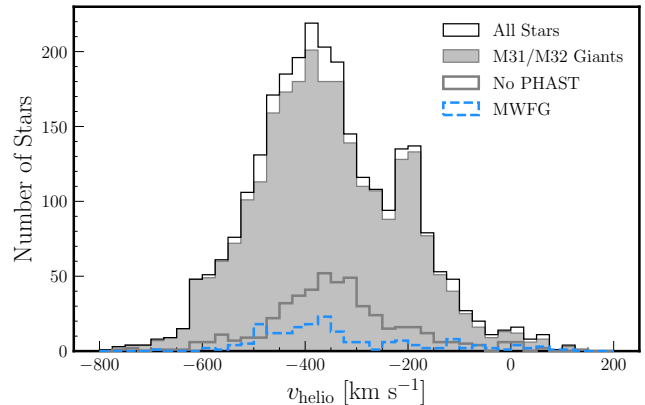


Figure 5. Velocity distributions for stars with successful velocity measurements (black outlined histogram; Section 2) and stars classified as M31/M32 giants (gray filled histogram; Section 3.1). Stars are present at very negative velocities ($v_{\text{helio}} < -500 \text{ km s}^{-1}$), where the systemic velocity of M31’s halo is -300 km s^{-1} . M31’s disk in the vicinity of M32 (Figure 6) exhibits a peak near -400 km s^{-1} and M32 itself is clearly visible as a peak near -200 km s^{-1} . The membership selection does not significantly alter the velocity distribution, including the tail toward MW-like velocities (near 0 km s^{-1}). We also show velocity distributions for stars without a photometric match in PHAST (gray outlined histogram) and stars assigned to the MW foreground (blue dashed histogram). Stars without photometry have velocities similar to M31’s disk/halo, whereas MW stars trace the disk (due to RHeB contamination) in addition to MW-like velocities.

MW foreground ($p_{M31+M32}$).⁶ In general, $p_{M31+M32}$ tends to decrease with increasing ΣNa (higher surface gravity) and decreasing ΣCa (lower metallicity). Some of the stars with MW-like velocities ($v_{\text{helio}} \gtrsim -100 \text{ km s}^{-1}$) have higher (lower) values of ΣNa (ΣCa) and therefore lower M31/M32 probabilities. However, the majority of stars have an overall high probability of being associated with M31 or M32, where the ΣCa and ΣNa distributions of stars at disk-like ($v_{\text{helio}} \sim -400 \text{ km s}^{-1}$; Dorman et al. 2012) and M32-like ($v_{\text{helio}} \sim -200 \text{ km s}^{-1}$) velocities appear indistinguishable. We classified 2525 stars with a higher likelihood of belonging to M31/M32 than the MW ($p_{M31+M32} > 0.5$) as giant stars.

The low contamination fraction of potential MW stars estimated from our sample (4.8%) is higher than expectations based on the predicted stellar density of the MW foreground relative to M31’s stellar disk and M32, but consistent given that our definition includes blue giant stars that are likely at M31 distances. Using the Be-

⁶ The distribution of EW_{Na} for M31 (the MW) in our model (Escala et al. 2020b) has $\langle \text{EW}_{\text{Na}} \rangle = 0.52 (3.07) \text{ \AA}$ and typical errors of $\langle \delta \text{EW}_{\text{Na}} \rangle = 1.06 (0.58) \text{ \AA}$.

sançon model⁷ (Robin et al. 2003), we simulated a population of MW contaminants over the area and magnitude range spanned by the DEIMOS data, assuming all ages, spectral types, and distances out to 150 kpc for MW stars. We used photometric transformations from Sirianni et al. 2005 to convert the output BVRI photometry to the ACS system. We calculated an expected MW contamination fraction of 0.2% over the portion of the PHAST CMD corresponding to M31/M32 giants, indicating that our membership determination is indeed conservative and that the impact of MW contamination on our sample is likely to be negligible.

We demonstrate the effect of the membership determination on the heliocentric velocity distribution (Section 2) in Figure 5, where the velocity structure remains largely unchanged between the distributions for all stars with successful velocity measurements and stars classified as M31/M32 giants. The presence of stars at MW-like velocities (near 0 km s⁻¹ in Figure 5) remains intact following the membership cut, implying that these stars may correspond to a genuine stellar population in the M31 system. Figure 5 also shows the velocity distributions for 549 M31/M32 giant stars without matched PHAST photometry and 121 stars classified as belonging to the MW foreground. The former population exhibits kinematics consistent with being concentrated in M31’s stellar disk or halo (where $v_{\text{sys},\text{M31}} \sim -300$ km s⁻¹), whereas the MW foreground stars are more evenly distributed in velocity. We discuss the velocity distribution structure of M31/M32 giants in more detail in Section 4.

3.2. Stellar Classification

We categorized M31/M32 giant stars into RGB and AGB stars based on their CMD positions (Figure 3). These stellar populations trace different mean ages, where RGB (AGB) stars in M32 are ~ 8.5 (4 ± 3) Gyr old (Monachesi et al. 2011, 2012). Moreover, the observed ratio of AGB to RGB stars in this region (Jones et al. 2023) indicates a similar average stellar age of 2–4 Gyr for stellar populations in both M32 and M31 (Monachesi et al. 2012; Bernard et al. 2015; Williams et al. 2015).

We defined the tip of the RGB (TRGB) using 12 Gyr HST/ACS PARSEC isochrones (Bressan et al. 2012) spanning $-2.2 < [M/H] < +0.5$ and a distance modulus of $\mu_{\text{M31}} = 24.45 \pm 0.05$ assuming that M31 and M32 are at the same distance (Savino et al. 2022). Although the light-weighted mean stellar age of M32 is 4.9 Gyr for all stellar populations (Monachesi et al. 2012) and equivalently 4 Gyr for RGB stars in M31’s disk (Williams et al.

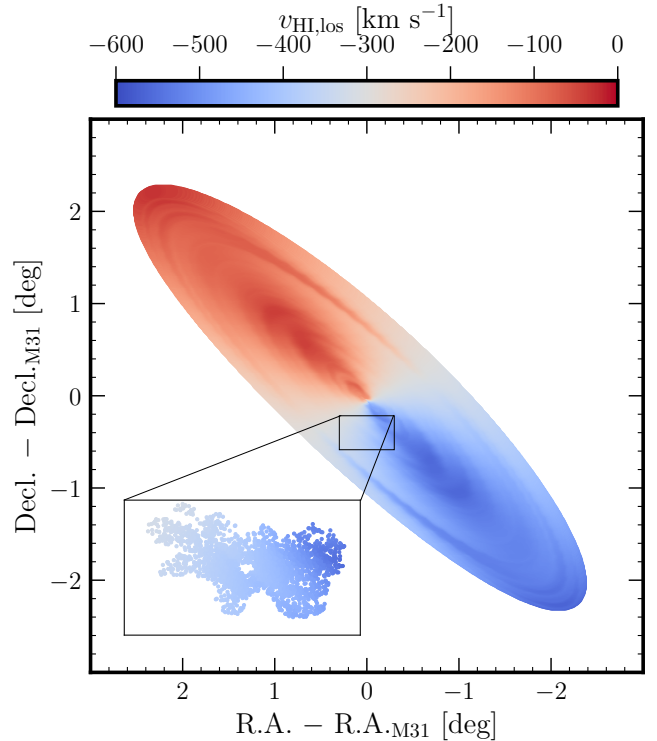


Figure 6. Predicted HI velocity of M31’s disk along the line-of-sight ($v_{\text{HI,los}}$) based on the tilted ring model and HI rotation curve from Chemin et al. (2009) (Section 4.1). The inset shows the DEIMOS footprint in the vicinity of M32 for stars with successful velocity measurements color-coded by $v_{\text{HI,los}}$. The median predicted $v_{\text{HI,los}}$ over this region is -389.2 km s⁻¹, where M31’s disk rotation speed varies from halo-like velocities (~ -300 km s⁻¹) to velocities characteristic of the southern half of M31’s disk (~ -500 km s⁻¹).

2015; Dorman et al. 2015), both systems show evidence of populations with ages at least 10 Gyr old (Fiorentino et al. 2012; Williams et al. 2017), motivating the use of the oldest reasonable isochrones to define the AGB, RGB, and MWFG stars to avoid bias against metal-poor populations. We assigned 1507 stars to the RGB given that they are below the TRGB within the photometric uncertainty: $m_{\text{F814W}} + \delta_{\text{F814W}} > m_{\text{TRGB}}$ (median $\delta_{\text{F814W}} = 0.006$). We assigned 536 stars above the TRGB but redder than the most metal-poor isochrone to the AGB. We discuss the AGB and RGB velocity distributions in Appendix A.3, where we consider the entire M31/M32 giant star velocity distribution in Section 4.

4. KINEMATICAL MODELING OF THE STELLAR OUTSKIRTS OF M32

In this section, we model the line-of-sight velocity distribution of the structurally complex region near M32 to isolate the kinematics of M32’s resolved stellar outskirts ($R_{\text{M32}} \gtrsim 1'$, or $\sim 2r_{\text{eff}}$). Previous kinematical studies of

⁷ https://model.obs-besancon.fr/modele_home.php

this region were based on smaller stellar sample sizes, were more limited spatial coverage, and relied on dividing the sample into spatial regions to account for the changing dynamical patterns of M31’s disk or M32 itself (Dorman et al. 2012; Howley et al. 2013). In contrast, we continuously model the kinematics of 2525 M31/M32 giant stars as a single region spanning 0.9–15.5 arcmin (or out to $\sim 23r_{\text{eff}}$ and $\sim 30r_{\text{eff}}$ along M32’s major/minor axes) by anchoring the rotation of M31’s disk to its HI kinematics, motivated by the formalism by Gilbert et al. (2022) and Cullinane et al. (2023).

We model the observed velocity distribution as a combination of stellar populations with kinematics tied to the rotation of M31’s gas disk and non-rotating populations with kinematics systematically offset from M31’s gas disk. The former “rotating” component captures the velocity distributions of, e.g., thin and thick stellar disks or potentially in-situ stellar halo components formed from the disk (c.f. Dorman et al. 2013; Gilbert et al. 2022; Escala et al. 2023; Cullinane et al. 2023), whereas the latter “offset” components describe the velocity distributions of dwarf galaxies such as M32, possible coherent tidal debris, or stellar halo components either formed ex-situ from accreted material or in-situ but exhibiting little to no rotation in the disk plane.

We present the model describing the rotation of M31’s stellar disk with respect to the gas in Section 4.1, where we detail our full “rotating plus offset” model in Section 4.2. We explore alternate models including multiple rotating components in Appendix A.2. We also consider separate “rotating plus offset” models with respect to stellar type (and therefore stellar age; Section 3.2) in Appendix A.3, where the kinematical parameters describing RGB and AGB populations broadly agree. We thus model the M31/M32 giant star velocity distribution as a whole to maximize our sample size and spatial coverage in the vicinity of M32 (Appendix A.3).

4.1. Tilted Ring Model for M31’s HI Disk

We described M31’s HI disk velocity using the tilted ring model of Chemin et al. (2009) (the adopted values in their Table 4), which provides HI rotation speed ($V_{\text{HI,rot}}$), position angle in degrees east of north (PA), and inclination (i) as a function of deprojected radius in M31’s disk plane (R_{disk}) between 0.4–38 kpc. For each star j , we calculated an initial R_{disk} estimate based on global values of M31’s disk inclination ($i = 77^\circ$) and position angle (PA = 38°), then interpolated within tilted ring model based on this initial R_{disk} value to assign each star an inclination i_j and position angle PA_j . We iteratively revised R_{disk} using the updated values of i_j and PA_j until convergence within 0.01° and 0.35° re-

spectively was achieved, following Gilbert et al. (2022) and Cullinane et al. (2023):

$$R_{\text{disk},j} = D_{\text{M31}} \sqrt{\alpha_j^2 + \left[\frac{\beta_j}{\cos(i_j)} \right]^2}, \quad (3)$$

$$\alpha_j = \eta_j \cos(\text{PA}_j) + \xi_j \sin(\text{PA}_j), \quad (4)$$

$$\beta_j = \xi_j \cos(\text{PA}_j) - \eta_j \sin(\text{PA}_j), \quad (5)$$

where (ξ, η) are the tangent-plane coordinates projected relative to M31’s center computed from sky coordinates (α, δ) and $D_{\text{M31}} = 776$ kpc (Savino et al. 2022). The line-of-sight component of the HI rotation velocity ($v_{\text{HI,los}}$) is therefore given by,

$$v_{\text{HI,los},j} = v_{\text{sys,M31}} + V_{\text{HI,rot}} \cos(\theta_j) \sin(i_j), \quad (6)$$

where $v_{\text{sys,M31}} = -300$ km s $^{-1}$ and θ_j is the azimuthal angle measured relative to the receding major axis of M31’s disk for a given star under the assumption that it is located in the disk plane,

$$\theta_j = \tan^{-1} \left[\frac{\beta_j}{\alpha_j \cos(i_j)} \right]. \quad (7)$$

Figure 6 shows $v_{\text{HI,los}}$ predicted by the Chemin et al. (2009) tilted ring model, where the rotation of HI gas in M31’s disk varies from M31 halo-like velocities (~ -300 km s $^{-1}$) to velocities characteristic of the southern half of M31’s disk (~ -500 km s $^{-1}$) over the DEIMOS footprint. The median predicted $v_{\text{HI,los}}$ over this region is -389.2 km s $^{-1}$. Given the substantial variation in line-of-sight velocity for M31’s HI disk, we anchored the predicted rotation of M31’s *stellar* disk to the gas, accounting for asymmetric drift by parameterizing the stellar disk rotation as a fraction of the HI (f_{rot}),

$$v_{\text{mod,los},j} = v_{\text{sys,M31}} + f_{\text{rot}} \times V_{\text{HI,rot}} \cos(\theta_j) \sin(i_j) \quad (8)$$

For each star, we then computed the offset between its observed and predicted line-of-sight velocity (Equation 8), $v_{\text{offset},j} = v_{\text{mod,los},j} - v_{\text{los},j}$. A stellar population rotating in the plane of M31’s HI disk at the HI rotation speed will have a v_{offset} distribution centered at 0 km s $^{-1}$ with an associated velocity dispersion. At the data location in the southern half of M31’s disk, stellar populations leading (lagging) the HI disk rotation will have positive (negative) v_{offset} values.

The top panel of Figure 7 shows the offset in observed heliocentric velocity for M31/M32 giant stars from the velocity predicted from the HI disk rotation (assuming $f_{\text{rot}} = 1$) as a function of sky position. In this disk-centric velocity frame, stars near the center of M32 lag

the rotation speed by $\sim 200 \text{ km s}^{-1}$ and are distinguishable from disk interlopers with $v_{\text{offset}} \sim 0 \text{ km s}^{-1}$. Moreover, trends between observed velocity and M31-centric major axis distance (R_{maj}) clearly demonstrate multiple stellar populations via M31’s rotation curve ($v_{\text{offset}} \sim 0 \text{ km s}^{-1}$), a cluster of stars corresponding to M32 ($R_{\text{maj}} \sim -5 \text{ kpc}$, $v_{\text{helio}} \sim -200 \text{ km s}^{-1}$), and velocity outliers in the v_{offset} distribution ($|v_{\text{offset}}| \gtrsim 400 \text{ km s}^{-1}$).

4.2. Rotating Plus Offset Model

Here, we model the velocity distribution of M31’s disk in the “rotating” velocity frame as a single kinematical component (Eq. 8) and any additional kinematical components in the “offset” or non-rotating heliocentric velocity frame, including an M31 halo-like component. We discuss alternate models that allow for multiple rotating M31 disk components and a rotating M31 halo-like component in Appendix A.2. The likelihood of our fiducial model is given by a sum of Gaussian components,

$$\mathcal{L} = \sum_j \left[\left(1 - \sum_N f_N \right) \times \mathcal{N}(v_{\text{offset},j}(f_{\text{rot}})|0, \sigma_{\text{disk}}) + \sum_N f_N \times \mathcal{N}(v_{\text{helio},j}|\mu_N, \sigma_N) \right], \quad (9)$$

where N is the number of offset model components, f , μ , and σ are the fractional contribution, mean velocity, and velocity dispersion of a given offset component, and σ_{disk} is the velocity dispersion of M31’s stellar disk. The probability that an individual star j is associated with a given offset component assuming the best-fit model parameters Θ is therefore,

$$p_{j,N} = \frac{f_N \times \mathcal{N}(v_{\text{helio},j}|\mu_N, \sigma_N)}{\mathcal{L}(\Theta)_j}, \quad (10)$$

and analogously for the rotating component in the v_{offset} velocity frame. We motivate the adopted number of model components and discuss their potential physical nature in Section 4.2.1 and describe the assumed priors on these components in Section 4.2.2. We present the best-fit kinematical parameters of the rotating plus offset model (Equation 9) in Section 4.2.3. We construct visualizations of the model (Figures 8, 12) by transforming the rotating component into the heliocentric velocity frame following Gilbert et al. (2022) (their Appendix B).

We acknowledge various caveats to our model, including the assumption that rotating model components do so in the disk plane, such that the model cannot adequately capture rotation in other planes. Owing to the tight coupling between the stellar and gas disks, the model also assumes that M31’s giant stars follow the same PA and inclination trends with radius as the HI

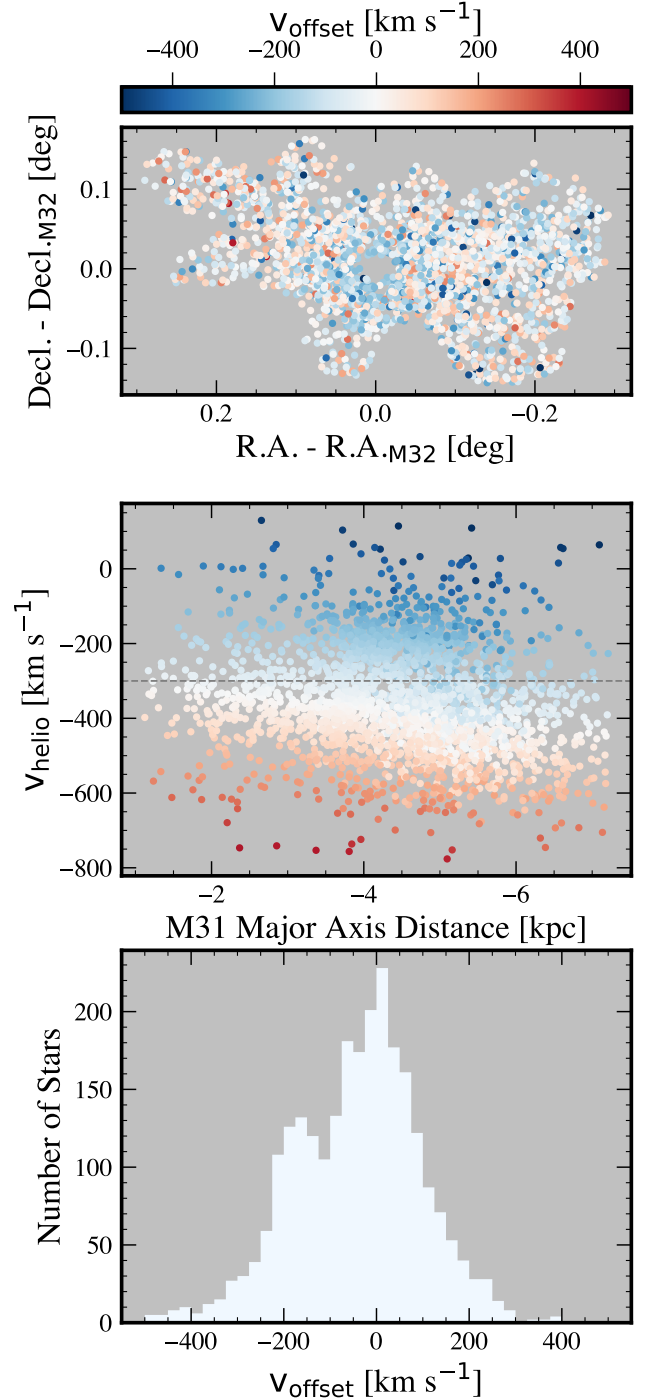


Figure 7. Offset in heliocentric velocity for giant stars near M32 from their predicted M31 HI disk velocity (v_{offset}) given the Chemin et al. (2009) tilted ring model (Figure 6; Section 4.1). (Top) M32-centric location color-coded by v_{offset} . (Middle) v_{helio} vs. M31-centric major axis distance color-coded by v_{offset} , where $v_{\text{sys},\text{M31}} = -300 \text{ km s}^{-1}$ (dashed line). The negative sign convention for the M31-centric major axis distance reflects the data location in the southern half of M31’s disk. (Bottom) v_{offset} distribution for M31/M32 giants assuming $f_{\text{rot}} = 1$ (light blue filled histogram). Stars with $v_{\text{offset}} \sim 0 \text{ km s}^{-1}$ have velocities near M31’s predicted disk rotation speed, and stars with $v_{\text{offset}} > 0 \text{ km s}^{-1}$ ($v_{\text{offset}} < 0 \text{ km s}^{-1}$) lead (lag) M31’s HI disk rotation. Stars near the center of M32 on the sky (and clustered near $R_{\text{maj}} \sim -5 \text{ kpc}$, $v_{\text{helio}} \sim -200 \text{ km s}^{-1}$) tend to lag the rotation speed by $\sim 200 \text{ km s}^{-1}$.

(Section 4.1) and have circular orbits. However, these limitations affecting the modeling of M31’s stellar disk are minimized by the small area covered by the data (Figure 1).

4.2.1. Number of Model Components

The structure of the velocity distributions in Figures 5 and 7 provides clear visual evidence for at least two kinematical components corresponding to M31’s disk and M32. However, we anticipate that M31’s stellar halo and bulge should also contribute to the stellar populations in this region (Section 2.1), whereas the non-negligible numbers of stars at the tails of the distribution in excess of expectations based on M31’s halo velocity dispersion (Section 4.2.2; Table 4.2.2) suggests the possible presence of additional kinematical components.

We estimated the marginal likelihood \mathcal{Z} of various N -component models given the data using the dynamic nested sampling implementation DYNESTY (Skilling et al. 2006; Higson et al. 2019; Speagle 2020),

$$\mathcal{Z} = \int \mathcal{L}(\Theta)\pi(\Theta)d\Theta, \quad (11)$$

where $\pi(\Theta)$ is the prior associated with the model parameters. We then compared the logarithm of the marginal likelihood ($\log_{10} \mathcal{Z}$) to evaluate the statistical evidence for increasing the number of components.

For this exercise, we assumed weakly informative uniform priors on all model parameters to remain relatively agnostic about the physical interpretation of each component. The first component, which is tied to M31’s HI gas rotation, corresponds to M31’s stellar disk, whereas all subsequent components are “offset” from the gaseous disk. We provide the details of the nested sampling implementation in Appendix A.1, which includes Table A.1 summarizing the comparison between various N -component models and Figure 12 showing the best-fit models compared to the observed velocity distribution.

With the weakly informative uniform priors, we found evidence for M31’s stellar disk and three offset components, or four total kinematical components. While the first offset component has high velocity dispersion ($\sigma_v \sim 120 \text{ km s}^{-1}$) similar to M31’s stellar halo (Dorman et al. 2012; Gilbert et al. 2018), it has a mean velocity ($\mu_v \sim -500 \text{ km s}^{-1}$) significantly offset from M31’s systemic velocity ($v_{\text{sys},\text{M31}} \sim -300 \text{ km s}^{-1}$), at odds with expectations for M31’s halo. The second offset component has a mean velocity close to M32’s systemic velocity (-200 km s^{-1}) and is kinematically cold similar to a dwarf galaxy. The third offset component ($\mu_v \sim -85 \text{ km s}^{-1}$, $\sigma_v \sim 90 \text{ km s}^{-1}$) accounts for stars at the positive tail of the velocity distribution. In this model, the stellar disk

slightly lags the gaseous disk ($f_{\text{rot}} \sim 0.8$) with a velocity dispersion ($\sigma_{\text{disk}} \sim 105 \text{ km s}^{-1}$) larger than expected for this region (Dorman et al. 2012).

The observed velocity distribution that we aim to model represents a structurally complex region on the sky, where the relative fraction of different model components changes significantly as a function of position. The combination of the complexity of the observed velocity distribution and the model assumption of weakly informative priors may therefore result in the attribution of stars belonging to one kinematical component to another. We thus explored the effect of separately modeling the kinematics of spatial regions near and far from M32 on the nature of the recovered model components, assuming the same weakly informative uniform priors as used in modeling the full dataset. We assigned M31/M32 giant stars with surface-brightness based M32 probability $p_{\text{M32,SB}} > 0.01$ to an “M32 Region” and stars with $p_{\text{M32,SB}} < 0.01$ to a “Disk Region” (Section 2.1).

Figure 8 shows the velocity distributions for these spatial regions, where the M32 region has two clear peaks corresponding to M31’s stellar disk and M32. Stars with M32-like velocities are still present in the disk region, demonstrating that M32’s velocity structure is likely to extend beyond the spatial region predicted by surface brightness alone. In the disk region, we identified M31’s stellar disk ($\sigma_v \sim 90 \text{ km s}^{-1}$), a kinematically hot component significantly offset from M31’s systemic velocity ($\mu_v \sim -400 \text{ km s}^{-1}$), and a kinematically hot component at the positive tail of the velocity distribution that is distinct from M32. This is qualitatively similar to the model components identified from the full dataset. In the M32 region, we found evidence for M31’s stellar disk ($\sigma_v \sim 45 \text{ km s}^{-1}$), a kinematically hot component with mean velocity close to M31’s systemic velocity, and a kinematically cold component with mean velocity close to M32’s systemic velocity (Table A.1; Figure 12). The presence a single kinematically hot component, as found in the M32 region, better conforms to expectations for M31’s stellar halo than the two kinematically hot components suggested by the disk region.

In choosing our fiducial model of one rotating component and four offset components, we combine the results of the above exercise with our existing knowledge of the properties of M31’s structural components, specifically its stellar halo and the presence of GSS-related tidal debris, derived from analyses covering much larger regions of M31 (Gilbert et al. 2009; Dorman et al. 2012; Gilbert et al. 2018). We thus interpret the two kinematically hot offset components preferred under the assumption of weakly informative priors as the likely superposition of three total components: an M31 halo-like component

Table 2. Normal Prior Parameters for “Offset” Model

Comp.	Parameter	Mean	Std.	Ref.
		[km s ⁻¹]	[km s ⁻¹]	
Disk	σ_{disk}	68.0	26.6	1
Halo-Like	f_v	0.45	0.05	1
	μ_v	-337.0	9.3	1,5
	σ_v	126.8	9.3	
M32	μ_v	-197.8	4.4	4,5
	σ_v	28.2	4.4	
MW-Like	μ_v	-55.9	8.8	2,5
	σ_v	44.2	8.8	
GSS-Like	μ_v	-618.0	8.8	3,6
	σ_v	30.0	8.8	

References. — (1) Dorman et al. (2012), (2) Gilbert et al. (2012), (3) Fardal et al. (2012), (4) H13, (5) Gilbert et al. (2018), (6) Escala et al. (2022). The priors for all other values of f_v (M32, MW-like, and GSS-like components), as well as for f_{rot} for M31’s disk, are uniform over the ranges [0,1] (f_v) and [0,1.5] (f_{rot}).

centered near M31’s systemic velocity plus two kinematically colder components at the positive (MW-like) and negative (GSS-like) velocity tails of the distribution (Section 4.2.2). Moreover, the fact that σ_{disk} decreases in accordance with literature expectations (Table A.1) when modeling the M32 and disk regions separately implies that weakly informative priors limit the ability of the model to disentangle between multiple distinct kinematical components. The results of this exercise based on weakly informative priors therefore indicates the need for more informative priors (Section 4.2.2).

Given the above arguments, we adopt a fiducial model consisting of five components—a rotating M31-disk like component and four offset non-rotating components—assuming informative priors on the model parameters for each component based on literature results (Section 4.2.2). However, in Section 4.2.3, we also explore the results of assuming fewer model components while retaining informative priors.

4.2.2. Normal Priors

We assumed normal priors on the mean velocity (μ_v) and velocity dispersion (σ_v) parameters fitted for each “rotating plus offset” velocity model (Table 3), where we summarize the adopted priors for each physically motivated kinematical component in Table 4.2.2. As discussed in Section 4.2.1 and Appendix A.1, we assumed five total kinematical components corresponding to M31’s stellar disk, a high velocity dispersion component similar to M31’s stellar halo, M32, and two components at the negative and positive velocity tails of the distribution with mean velocities similar to expectations for GSS-related tidal debris in this region and the MW

foreground population (although not necessarily associated with either population).

For the stellar disk of M31, we assumed uniform priors on f_{rot} between 0 and 1.5 to allow the model to explore rotation speeds from those approaching zero to speeds similar to or slightly faster than predicted from the HI. We computed the Gaussian prior on σ_{disk} from an average of the disk dispersion parameters derived by Dorman et al. (2012) in their “SSW” region corresponding to the H13 spectroscopic sample, where we excluded the anomalously low dispersion value fitted in the angular subregion containing M32 (their Table 4).

For the halo-like component, we calculated the priors on μ_v and σ_v from a simple average of two sources: (1) the kinematical M31 spheroid parameters from Dorman et al. (2012) for the entire SSW region corrected for tidal debris (their Table 3), and (2) the kinematical stellar halo parameters for projected M31-centric radii between 8–14 kpc from Gilbert et al. (2018), which we transformed from the galactocentric to the heliocentric frame based on the mean R.A. and Decl. of our sample (van der Marel & Guhathakurta 2008; van der Marel et al. 2012). This assumes that M31’s stellar halo exhibits similar dynamical behavior at our data location ($R_{\text{proj},\text{M31}} \sim 3.4\text{--}7.7$ kpc) compared to 8–14 kpc.

We also implemented a normal prior on the fractional contribution (f_v) of the halo-like component in the 5D model (Section 4.2.1) based on the simple mean of f_v values in the SSW region of Dorman et al. (2012) (again excluding the subregion containing M32). Without this constraint on the prior, the fitting procedure prefers a model where $f_{v,\text{halo}} \sim 5\%$ (in contrast to the f_v values suggested by all other models in Table 3, as well as previous literature results based on the H13 subsample) in favor of increasing the disk dispersion to $\sigma_{v,\text{disk}} \sim 110$ km s⁻¹ and decreasing the disk rotation speed to $f_{\text{rot}} \sim 0.8$. Interestingly, the data prefer a substantial M31 halo-like contribution in the vicinity of M32, despite surface-brightness based predictions from structural decomposition in M31’s northeast implying an M31 halo-like contribution of 7.4% (for the combination of M31’s stellar halo and bulge over the survey area; Section 2.1).

The priors for M32 are based on a simple average of the values from Dorman et al. (2012) (their Table 4) and H13. For the MW-like component at the positive tail of the velocity distribution, we adopted values based on the mean and standard deviation of the line-of-sight velocity distribution for securely identified MW stars in the SPLASH survey of M31’s southeastern minor axis (Gilbert et al. 2012, 2018). We relied on this empirical distribution rather than model predictions for the MW foreground at the data location (e.g., Robin et al. 2003;

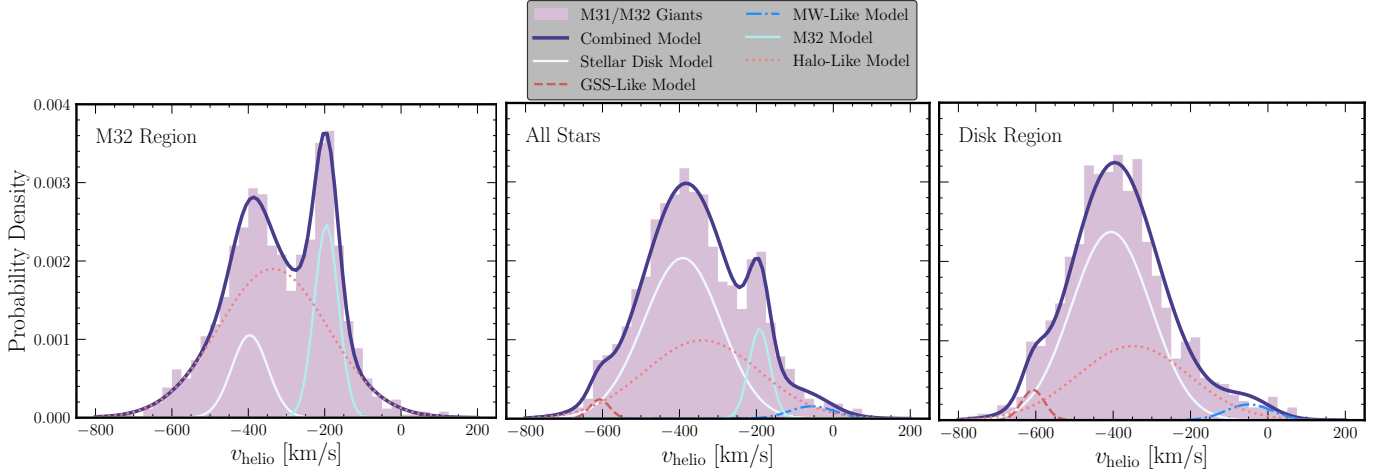


Figure 8. Observed velocity distributions for M31/M32 giant stars compared to best-fit velocity models assuming normal priors (Table 4.2.2), where the models consist of a component rotating in the velocity frame relative to M31’s disk (v_{offset} ; Figure 7) at some fraction of the predicted rotation speed (“Stellar Disk Model”) and multiple components offset from the rotating component in the heliocentric velocity frame (Section 4.2; Table 3). We show best fit models for giant stars near M32 (left panel; $p_{\text{M32,SB}} > 0.01$; Figure 2), away from M32 (right panel; $p_{\text{M32,SB}} < 0.01$), and all giant stars (middle panel). We find evidence for four total “offset” components corresponding to M32, two populations with MW-like and GSS-like mean velocities respectively (although not necessarily associated with these structures), and an M31 halo-like population with high velocity dispersion. Stars with M32-like velocities ($\sim -200 \text{ km s}^{-1}$) are still present in the “Disk Region”, demonstrating that M32 velocity structure extends beyond the region predicted by surface brightness alone.

Table 3. Kinematical Parameters for Rotating Plus Offset Model – Normal Priors

Model	f_{rot}	$\sigma_{\text{disk}} [\text{km s}^{-1}]$	Comp.	f_v	$\mu_v [\text{km s}^{-1}]$	$\sigma_v [\text{km s}^{-1}]$
	Disk		Offset Components			
Preferred Model, All Stars						
5D*	$0.96^{+0.02}_{-0.04}$	$91.8^{+3.0}_{-7.0}$	Halo-Like	$0.37^{+0.02}_{-0.05}$	$-340.9^{+4.5}_{-10.1}$	$148.9^{+2.9}_{-6.4}$
			M32	$0.08^{+0.01}_{-0.01}$	$-191.9^{+1.4}_{-3.3}$	$27.5^{+1.5}_{-3.3}$
			MW-Like	$0.02^{+0.00}_{-0.01}$	$-55.5^{+4.4}_{-8.9}$	$58.9^{+3.6}_{-9.0}$
			GSS-Like	$0.02^{+0.00}_{-0.01}$	$-607.5^{+3.1}_{-7.4}$	$25.8^{+2.7}_{-6.4}$
Alternative Model, All Stars						
3D	$0.98^{+0.02}_{-0.04}$	$96.2^{+2.4}_{-5.9}$	Halo-Like	$0.42^{+0.02}_{-0.04}$	$-329.9^{+3.0}_{-6.7}$	$159.7^{+1.9}_{-4.2}$
			M32	$0.07^{+0.01}_{-0.01}$	$-191.7^{+1.4}_{-3.1}$	$25.8^{+1.6}_{-3.4}$
Disk Region, $p_{\text{M32,SB}} < 0.01$						
4D	$0.97^{+0.02}_{-0.05}$	$88.1^{+3.1}_{-6.9}$	Halo-Like	$0.34^{+0.03}_{-0.07}$	$-348.0^{+4.1}_{-8.9}$	$143.9^{+3.1}_{-8.3}$
			MW-Like	$0.03^{+0.00}_{-0.01}$	$-48.6^{+3.9}_{-8.4}$	$59.0^{+3.0}_{-7.9}$
			GSS-Like	$0.03^{+0.01}_{-0.01}$	$-607.0^{+2.9}_{-8.3}$	$29.4^{+4.5}_{-8.7}$
M32 Region, $p_{\text{M32,SB}} > 0.01$						
3D	$1.18^{+0.05}_{-0.13}$	$45.4^{+6.3}_{-13.0}$	Halo-Like	$0.68^{+0.03}_{-0.07}$	$-334.9^{+2.8}_{-6.3}$	$143.0^{+2.1}_{-4.3}$
			M32	$0.19^{+0.01}_{-0.03}$	$-195.6^{+1.4}_{-3.2}$	$31.5^{+1.4}_{-3.2}$

* The fiducial 5D model (Section 4.2.3) for all M31/M32 giant stars is adopted for the analysis of M32’s kinematics in Section 5.

Section 3.1) because the observed distribution of MW stars is known to differ owing to the selection function of our surveys (Gilbert et al. 2018). The standard deviations on the priors for the MW-like (and GSS-like) component(s) are equivalent to twice that of the M32 priors (4.4 km s^{-1}), which is approximately the median velocity uncertainty of our sample (4.2 km s^{-1}).

We based the priors for the ‘‘GSS-like’’ component on N-body model predictions for the velocity distribution of satellite tidal debris from the GSS merger event at the data location (Escala et al. 2022). In this model, the GSS and its associated tidal shells form from a progenitor with stellar mass $M_{\text{sat}} = 2.2 \times 10^9 M_{\odot}$ that completely disrupted 0.8 Gyr ago, where this model broadly reproduces the observed properties of M31’s major system of tidal features (Fardal et al. 2007, 2012, 2013; Gilbert et al. 2007; Escala et al. 2022). In Appendix B, we show the predicted debris pattern in projected phase space compared to the observed distribution of M31/M32 giants. Although the model predicts M31 to dominate the stars in this region, GSS-related tidal debris should be most detectable near -600 km s^{-1} , where stars with such negative velocities are present in our dataset. Moreover, the predicted debris also extends to positive MW-like velocities (near 0 km s^{-1}).

We isolated the dominant tidal feature in the model using a two-component variational Bayesian Gaussian mixture (Pedregosa et al. 2011), where the predicted stream has $\mu_v \sim -618 \text{ km s}^{-1}$ and $\sigma_v \sim 30 \text{ km s}^{-1}$ (Table 4.2.2). Despite being limited to a single model in a specific merger scenario, this theoretical constraint is useful for evaluating the statistical significance of the identification of a stellar population potentially originating from the GSS progenitor.

4.2.3. Resulting Velocity Models

We sampled the posterior distribution of the model parameters using the dynamic nested sampling implementation DYNESTY (Speagle 2020) in order to maximize the logarithm of the model likelihood (Equation 10). We present the best-fit kinematical parameters for ‘‘rotating plus offset’’ models assuming 5 total components across the entire spectroscopic sample (Section 4.2.1) in Table 3, where parameter values are based on the 16th, 50th, and 84th percentiles of the marginalized posterior probability distribution. The offset model components consist of M32, a high-dispersion M31 halo-like population, and two components at GSS-like and MW-like velocities (Section 4.2.2). Figure 8 shows the best-fit models for giant stars near M32 ($p_{\text{M32,SB}} > 0.01$), away from M32 ($p_{\text{M32,SB}} < 0.01$), and all giant stars covering the region spanned by our entire dataset.

For all M31/M32 giant stars, M32 contributes $\sim 8\%$ of the stars in the sample with $\mu_{v,\text{M32}} \sim -191.7_{-3.3}^{+1.4} \text{ km s}^{-1}$ and $\sigma_{v,\text{M32}} \sim 25.8_{-3.4}^{+1.6} \text{ km s}^{-1}$, consistent with the results of restricting the model to the region near M32.

Across all spatial regions, we found consistent values for the M31 halo-like component of $\mu_v \sim -340 \text{ km s}^{-1}$ and $\sigma_v \sim 145 \text{ km s}^{-1}$, which contributes $\sim 35\%$ of the stars when considering a more globally representative sample that includes stars away from the M32 region. M31’s stellar disk rotates with speeds similar to the gas ($f_{\text{rot}} \sim 1$) and a dispersion of $\sim 90 \text{ km s}^{-1}$, though we find a faster rotation speed and smaller dispersion for the portion of the disk in the localized region near M32 (similar to the results of Dorman et al. 2012).

We also found evidence for small contributions (at the $\sim 2\%$ level) from populations with GSS-like and MW-like velocities when considering spatial regions containing stars with low prior probability of belonging to M32. We assessed whether including the GSS-like and MW-like model components indeed provides a better description of the data by comparing the fiducial 5D model to a 3D model including only M31’s stellar disk, an M31 halo-like component, and M32 (Table 3). The 3D model provides a worse description of the data ($\Delta \log \mathcal{Z} \sim -1.1$). Regardless of whether we included GSS-like or MW-like components, the M32 kinematical parameters are consistent between the 3D and 5D models in Table 3.

Despite the presence of stars with velocities near -600 km s^{-1} and 0 km s^{-1} (Figure 8), we do not detect GSS-like or MW-like populations at a statistically significant level in the M32 region, likely owing to the restricted coverage of this subsample. We confirmed that including a GSS-like or MW-like component is not preferred over a model excluding these components in the M32 region ($\Delta \log \mathcal{Z} < -2$). In Section 5, we base the analysis of M32’s kinematics on the fiducial 5D model for all M31/M32 giant stars, which provides the best statistical description of the data over the largest area.

5. KINEMATICAL PROPERTIES OF STELLAR POPULATIONS IN M32

Here, we explore M32’s internal dynamical properties in the context of our spatially continuous model (Section 4) for the line-of-sight velocity distribution on this region of the sky. In Section 5.1, we search for differences in the structure of M32’s probabilistically extracted velocity distribution between its ‘‘inner’’ and ‘‘outer’’ regions, separated by the radius at which M32’s isophotal contours in its surface brightness profile are observed to twist along its major axis ($R_{\text{iso}} \sim 150'' \sim 0.56 \text{ kpc}$; Figure 2; C02). We model the rotational behavior of M32’s inner and outer regions in Section 5.2 and construct on-

sky maps of M32’s predicted velocity structure enabled by our modeling approach in Section 5.3.

Throughout this section, we use the surface-brightness based M32 probability ($p_{M32,SB}$; Section 2.1) only as a guide on where to expect M32 stars compared to predictions from kinematics. As noted by H13, the idealized 2D surface brightness model may not accurately capture non-uniform deviations in the surface brightness of M31’s disk, or may reflect an excessively steep surface brightness profile for M32. Moreover, the global surface brightness model for M31 is based on constraints from the northeast (Dorman et al. 2013), and may not be representative of the region of the sky near M32.

5.1. M32’s Line-of-Sight Velocity Distribution

Prior studies with more limited sample size and coverage, as well as distinct modeling approaches, found that M32’s kinematics appeared symmetric and without clear evidence of sharp gradients across the region defined by M32’s isophotal elongation (H13). We thus revisit M32’s kinematical properties with respect to R_{iso} in light of our improved sample size and coverage and updated statistical methodology.

Figure 9 shows the velocity distributions for M32’s inner and outer regions, constructed by weighting the observed line-of-sight velocities by their position and velocity based probabilities of belonging to M32 (Equation 10; Section 4.2.3). We show velocity distributions for M32 extracted using probabilities from solely the kinematical model ($p_{M32,vel}$) and the combination of the kinematical plus surface-brightness models ($p_{M32,vel} \times p_{M32,SB}$). Regardless of whether surface-brightness information is included, M32’s predicted velocity structure does not substantially change for M32’s inner regions. In contrast, the model including surface-brightness information predicts that M32’s outer velocity distribution has more stars toward the negative tail and is marginally more centrally concentrated compared to the case without surface-brightness information. As shown in Section 4.2.1, photometry alone predicts fewer stars at larger M32-centric radii compared to kinematics (see also H13), thereby decreasing the probability of belonging to M32 beyond R_{iso} . Given that our goal is to constrain M32’s kinematical structure in its outskirts, we therefore focus on predictions based solely on $p_{M32,vel}$.

Figure 9 further demonstrates that M32’s velocity structure changes between its inner and outer regions. Inside the isophotal twisting radius, M32 has a velocity distribution characterized by negative kurtosis, or a centrally concentrated flat peak with few outliers, that results from M32’s ordered rotation. Beyond this radius, M32’s velocity distribution is asymmetric with

positive kurtosis, indicating a centrally concentrated peak with heavier outliers. We quantified the change in M32’s velocity structure by computing the moments of the distributions based on 1000 Monte-Carlo bootstrap trials. We perturbed the sample velocities assuming Gaussian velocity uncertainties, then re-computed the velocity distribution, weighting each velocity measurement by $p_{M32,vel}$, and measured the moments of the resulting bootstrapped distribution. We computed the median values and the uncertainties based on the 16th, 50th, and 84th percentiles of this distribution. For $R_{proj,M32} < R_{iso}$, we obtained $\mu_v = -189.6^{+0.5}_{-0.4}$ km s⁻¹, $\sigma_v = 25.7^{+2.4}_{-0.4}$ km s⁻¹, $\gamma_v = 0.0 \pm 0.03$, and $\kappa_v = -0.29^{+0.12}_{-0.08}$ for the mean, standard deviation, skewness, and excess kurtosis respectively. For $R_{proj,M32} > R_{iso}$, we found $\mu_v = -190.8 \pm 0.4$ km s⁻¹, $\sigma_v = 28.7^{+1.3}_{-0.4}$ km s⁻¹, $\gamma_v = 0.03 \pm 0.03$, and $\kappa_v = +0.15 \pm 0.07$. Although μ_v and σ_v are unchanged with respect to R_{iso} κ_v differs by $\gtrsim 3\sigma$. When considered with M32’s other internal kinematical properties (Section 5.2), we interpret this change in kinematical structure as evidence in favor of tidal distortions affecting M32 (Section 6).

For reference, we also show M32’s escape velocity at $R_{proj,M32} = 200''$ in Figure 9, which was calculated from a three-integral Schwarzschild orbit model for M32’s mass distribution fitted to a combination of integrated-light and resolved stellar kinematics by H13 ($v_{M32} \pm 72$ km s⁻¹, where we adopt v_{M32} from Table 3). The probability density of the predicted velocity distribution approaches zero near this escape velocity, although some velocity structure remains present beyond this boundary. We estimated the predicted fraction of stars beyond this velocity using Gaussian kernel density estimates of M32’s line-of-sight velocity distribution (as in Figure 9), which are weighted by the inverse square of the velocity measurement uncertainty and the probability of belonging to M32 ($p_{M32,vel}$).

We found that approximately 3.6% of stars (4.7% when incorporating $p_{M32,SB}$) associated with M32 in our model beyond 200'' may have velocities beyond the escape velocity, in qualitative agreement with the findings of H13 that stars potentially associated with M32 are present beyond this limit. If these stars beyond the isophotal twisting radius and the escape velocity are bound to M32, H13 interpreted them as possible evidence of a dark matter halo, non-equilibrium tidal distortions in M32’s outskirts, or M31 substructure. However, they found the explanation of a dark matter halo less likely given M32’s asymmetric velocity distribution, where the excess of fast-moving stars at large radii were preferentially detected toward M32’s positive velocity tail ($\sim 1.3\%$ out of $\sim 2.9\%$ of stars beyond 200'' in

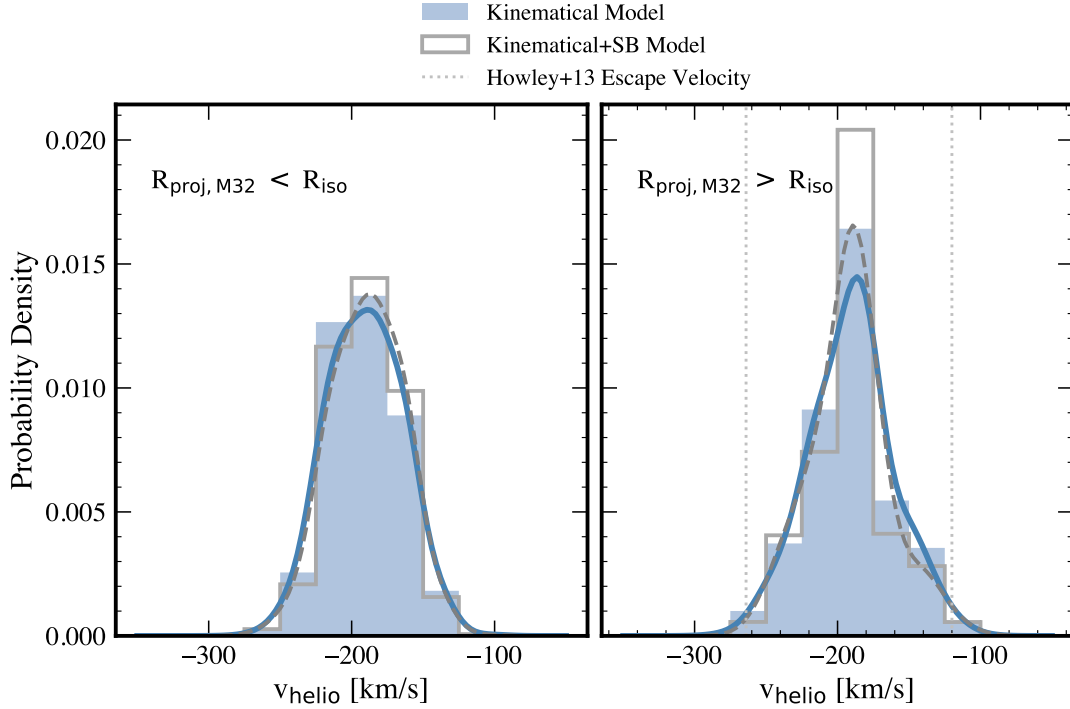


Figure 9. Velocity distributions for M32’s inner (left panel) and outer regions (right panel), separated by the isophotal twisting radius ($R_{\text{iso}} \sim 150''$). We show histograms of stellar velocities weighted by M32 probability, based on kinematics alone ($p_{\text{M32,vel}}$, blue histograms) and including surface brightness information ($p_{\text{M32,vel}} \times p_{\text{M32,SB}}$, grey histograms), and also weighted by the inverse square of the velocity measurement uncertainty. We also show corresponding Gaussian kernel density estimates (blue solid lines and grey dashed lines, respectively). For reference, we include M32’s escape velocity at $200''$ in the equatorial plane calculated from a three-integral model by H13 ($v_{\text{M32}} \pm 72 \text{ km s}^{-1}$) in the right panel. Beyond the twisting radius, M32 has a more sharply peaked velocity distribution with heavier outliers, whereas the velocity distribution within R_{iso} is flatter with fewer outliers as a consequence of M32’s ordered rotation.

our model when assuming $v_{\text{M32}} = -201 \text{ km s}^{-1}$ as in H13). We further discuss these hypotheses for explaining M32’s observed kinematics in Section 6.

5.2. Rotation in M32

M32 is known to possess a steep rotational velocity gradient at its center driven by a central black hole ($M_{\text{BH}} \sim 2 - 4 \times 10^6 M_{\odot}$; e.g., Bender et al. 1996; van der Marel et al. 1997, 1998; Joseph et al. 2001; Verolme et al. 2002; van den Bosch & de Zeeuw 2010). M32’s rotational velocity falls from maximum value of $v_{\text{max}} \sim 46 \text{ km s}^{-1}$ at a radius of $\sim 1''$ (4 pc) along its major axis before flattening at $\sim 10 \text{ km s}^{-1}$ beyond $\sim 100''$ or 0.4 kpc, whereas no clear line-of-sight velocity trends have been detected along its minor axis (H13). We therefore modeled M32’s rotation based on our computed M32 probabilities ($p_{\text{M32,vel}}$; Equation 10), separately considering populations located inside and outside of M32’s isophotal twisting radius. The likelihood function describing the observed line-of-sight velocity due to M32’s

azimuthally uniform rotation is,

$$\begin{aligned} \mathcal{L}_j &= \mathcal{N}(v_{\text{helio},j} | \mu_{\text{M32}} - k_R \cos(\theta_R - \theta_j), \sigma_{\text{M32}}), \\ \log \mathcal{L} &= \sum_j p_{\text{M32,vel},j} \times \log \mathcal{L}_j \end{aligned} \quad (12)$$

where k_R is the rotation magnitude, θ_R is the position angle representing the rotation direction in degrees east of north, and μ_{M32} and σ_{M32} are the adopted parameters describing M32’s velocity distribution from Table 3.

We followed the procedure detailed in Section 4.2.3 to sample the associated posterior probability distribution, assuming a normal prior of $\mathcal{N}(10, 4.4)$ on k_R , based on the major-axis rotational profile of H13 at large radii (their Figure 10) and our typical velocity uncertainty (Table 4.2.2), and a uniform prior bounded by $[0, 2\pi]$ on θ_R (which we converted to degrees after sampling). We found best-fit values of $k_R = 7.0_{-3.9}^{+1.6} \text{ km s}^{-1}$ and $\theta_R = -31.2_{-59.4}^{+24.7} \text{ deg E of N}$ for the rotational velocity magnitude and direction respectively within R_{iso} ($k_R = 5.3_{-3.2}^{+1.3} \text{ km s}^{-1}$ and $\theta_R = -126.4_{-58.9}^{+27.4} \text{ deg E of N}$ outside of R_{iso}).

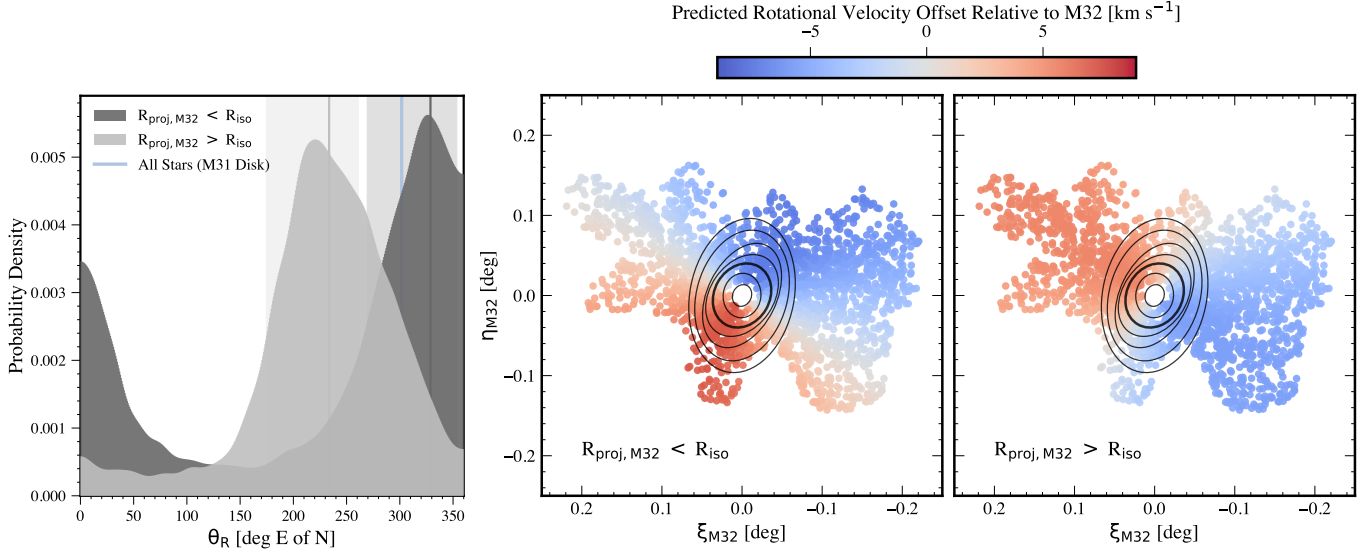


Figure 10. Rotational model parameters describing M32’s line-of-sight velocity distribution (Equation 12; Section 5.2), derived by weighting by the probability of belonging to M32 ($p_{\text{M32,vel}}$). (Left panel) Marginalized posterior probability distributions for the rotational direction (θ_R) within (dark grey) and outside of (light grey) the isophotal twisting radius (R_{iso}), with vertical lines showing median values and shaded regions showing 1σ confidence intervals. We also show θ_R for all M31/M32 giant stars (i. e., unweighted by $p_{\text{M32,vel}}$), which corresponds to a population dominated by M31’s disk (solid blue line). (Right panels) M32-centric location of each star in our dataset color-coded by its predicted velocity offset, due to M32’s rotation, from the mean velocity of M32 (Table 3). We also show the I-band isophotes from C02 for reference, with R_{iso} bolded (black ellipses). The orientation of the rotation (or linear velocity gradient; see Section 5.2) shifts direction from the region inside and outside R_{iso} ; within R_{iso} , the rotation is approximately aligned along M32’s major axis ($\theta_{R,\text{inner}} \sim -30$; receding from NNW to SSE, as expected), whereas outside R_{iso} the change in velocity is aligned roughly along M32’s minor axis ($\theta_{R,\text{outer}} \sim -130$; receding from WSW to ENE). This direction is distinct from that of the rotation of M31’s disk over the data footprint ($\theta_{R,\text{disk}} \sim -60$; receding from NW to SE; Figure 6).

The rotational velocity magnitude for both M32’s inner and outer region is consistent within the uncertainties with previous results from binned spatial regions in M32’s outskirts along its major axis from H13. Although the errors on the rotational direction are large, the marginalized posterior probability distributions have shapes similar to skewed Gaussians that are clearly peaked about the median values (Figure 10). Moreover, the best-fit value of θ_R within R_{iso} is close to M32’s major axis direction (roughly -22 deg E of N; C02) as expected, despite the fact that we used uniform priors on θ_R . This supports the interpretation that the true value of the maximal rotation direction is likely accurately, albeit imprecisely, recovered by our model.

Figure 10 shows the velocity offset, due to M32’s rotation, from M32’s mean velocity (Equation 12) predicted over the data footprint both inside and outside of R_{iso} , color-coded by the value assigned to each star assuming it belongs to M32. The orientation of M32’s rotation between its inner and outer regions is predicted to change: the line-of-sight velocity shifts from increasing from NNW to SSE along M32’s major axis within R_{iso} , to increasing from WSW to ENE along M32’s minor axis outside of R_{iso} . Despite the large uncertainties in θ_R ,

the values for $\theta_{R,\text{inner}}$ and $\theta_{R,\text{outer}}$ are non-overlapping within the 1σ confidence intervals (Figure 10). This supports the statistical significance of a change in the rotational direction when considered with the fact that the model is able to accurately recover M32’s major-axis rotation within R_{iso} .

As noted in the case of Milky Way satellite dwarf galaxies that are likely tidally disrupted (e.g., Ji et al. 2020), it is not necessarily straightforward to disentangle observational signatures of rotation from tidally induced linear velocity gradients owing to the similar functional forms when modeling line-of-sight velocity distributions (Walker et al. 2016; Caldwell et al. 2017). This raises the question of whether the change in θ_R between M32’s inner and outer regions indeed reflects a change in M32’s rotation direction, or a transition to a regime characterized by tidal distortions, as opposed to ordered rotation, that coincides with M32’s isophotal elongation. To demonstrate this, we modified Equation 12 to depend on the projected distance from the center of M32 (R_{M32}),

$$\mathcal{N}(v_{\text{helio}}, j | \mu_{\text{M32}} - k_V R_{\text{M32}} \cos(\theta_V - \theta_j), \sigma_{\text{M32}}), \quad (13)$$

where k_V and θ_V correspond to the magnitude and direction of the linear velocity gradient respectively.

Assuming that M32 rotates at $v_{\text{rot}} \sim 10 \text{ km s}^{-1}$ over a region encompassed by $|R_{\text{M32}}| < 1 \text{ kpc}$ (approximately twice R_{iso}) similarly yields an expected prior on k_V of $\mathcal{N}(10, 4.4)$ for the velocity gradient magnitude. From sampling the posterior distribution, we obtain a weak gradient of $k_V = 3.5_{-2.8}^{+1.2} \text{ km s}^{-1} \text{ kpc}^{-1}$ and $\theta_V = -146.0_{-75.4}^{+41.6} \text{ deg E of N}$ for $R_{\text{proj}, \text{M32}} > R_{\text{iso}}$. These model parameters produce a similar predicted line-of-sight velocity pattern on the sky compared to the rotational model, supporting the notion that M32’s detected rotation beyond the isophotal twisting radius can be reasonably modeled as a weak linear velocity gradient.

The shift in M32’s rotational direction with respect to R_{iso} may be a kinematical signature of tidal distortion (Section 6), but could also originate from contamination by rotating stellar populations distinct from M32 that become more dominant at large M32-centric radii. For example, M31’s disk exhibits significant rotation over the data footprint (Figure 6; Section 4.1), and M31’s inner stellar halo is also known to rotate at $V_{\text{rot}, \text{halo}} = 52.6 \pm 6.8 \text{ km s}^{-1}$ for $R_{\text{proj}, \text{M31}} > 5 \text{ kpc}$ in approximately the same direction as M31’s disk (Dorman et al. 2012; Appendix A.2).

We therefore tested whether $\theta_{R, \text{outer}}$ is distinct from the sense of M31’s disk/halo rotation ($\theta_{R, \text{disk}}$) by sampling the posterior distribution of Equation 12 *without* weighting by $p_{\text{M32}, \text{vel}}$, where our sample is dominated by stars in M31’s disk and halo-like populations ($\sim 88\%$ of the sample; Table 3). Assuming uniform priors on both parameters, we measured $k_{R, \text{disk}} = 89.2_{-0.9}^{+0.4} \text{ km s}^{-1}$ $\theta_{R, \text{disk}} = -58.3_{-0.6}^{+0.2} \text{ deg E of N}$, corresponding to a strong disk rotational signature over the data footprint. This orientation is similar to that of M32 within R_{iso} , where both $\theta_{R, \text{inner}}$ and $\theta_{R, \text{disk}}$ are receding towards the northwest, whereas the direction for M32 beyond R_{iso} ($\theta_{R, \text{outer}}$) recedes to the southwest. We thus conclude that the shift in M32’s rotational direction with R_{iso} is unlikely to be driven by contamination from M31’s disk or halo, given that the distinct orientation of M32’s rotation beyond the isophotal twisting radius ($\theta_{R, \text{outer}} = -126.4_{-58.9}^{+27.4} \text{ deg E of N}$) cannot be produced by a summation of M32’s inner rotation and M31 contamination.

5.3. Predicted Structural Maps of M32

We constructed 2D maps of M32’s structure on the sky predicted by our spatially continuous “rotating plus off-set” model from Section 4.2. The upper left panel of Figure 11 shows the location of all M31/M32 giants in our dataset color-coded by the likelihood-based probability of belonging to M32 computed from the spatial positions and line-of-sight velocities of individual stars ($p_{\text{M32}, \text{vel}}$; Equation 10). Despite the fact that the kinematical

model does not incorporate information on M32’s sky location (Section 4.2), stars near the center of M32 have the highest probability of being members of the dwarf galaxy, although some stars with M32-like velocities are present at large M32-centric radii.

We approximated the probability density function (PDF) of M32’s spatial distribution using a Gaussian kernel density estimate weighted according to $p_{\text{M32}, \text{vel}}$ and the inverse square of the velocity measurement uncertainty. The resulting map in the upper middle panel of Figure 11 shows that the kinematical model predicts faint stellar structures associated with M32 beyond its outermost I-band isophote (C02), which appear as elongations NE (SW) in M32’s north (south).⁸

These potential structures could result from contamination by stars in M31’s disk and/or halo with M32-like velocities that were incorrectly attributed to M32 by the model. However, given that the model explicitly accounts for the line-of-sight velocity variation of M31’s disk, we do not expect M31’s disk to be a significant source of contamination, particularly west of M32 where M31’s disk has more negative predicted velocities relative to M32 (Figure 6). Moreover, the shapes of the putative structures to the NE and SW of M32 beyond the outermost isophote could reflect the data footprint or selection function (Section 2) instead of M32’s underlying stellar density distribution.

To evaluate the robustness of the features compared to the data footprint, we constructed maps of the residuals between PDFs for M32 and the full dataset of M31/M32 giant stars (i.e., between PDFs weighted and unweighted by $p_{\text{M32}, \text{vel}}$). The upper right panel of Figure 11 shows that M32 is preferentially detected toward the southeast (in the direction away from M31; Figure 1) and largely within R_{iso} . The model also preferentially removes stars to the west of M32, where the velocity difference between M31’s disk and M32 is the largest ($\mu_{v, \text{disk}} \sim -500 \text{ km s}^{-1}$ vs. $\mu_{v, \text{M32}} \sim -200 \text{ km s}^{-1}$; Figure 6). Figure 11 also illustrates that elongations in M32’s predicted stellar structure beyond the outermost isophote remain present in the NE–SW direction, albeit more tentatively so in the NE. Interestingly, this direction roughly corresponds to M32’s minor axis and therefore the change in orientation of M32’s rotational velocity signature beyond R_{iso} (Section 5.2, see also 6).

The bottom panels of Figure 11 are the same as the top panels, except using M32 probabilities including

⁸ Although no data is present in M32’s central regions (left panels of Figure 11), the PDF and associated residual maps (center and right panels of Figure 11) are non-zero, albeit still low density, at their centers as a consequence of the Gaussian kernel.

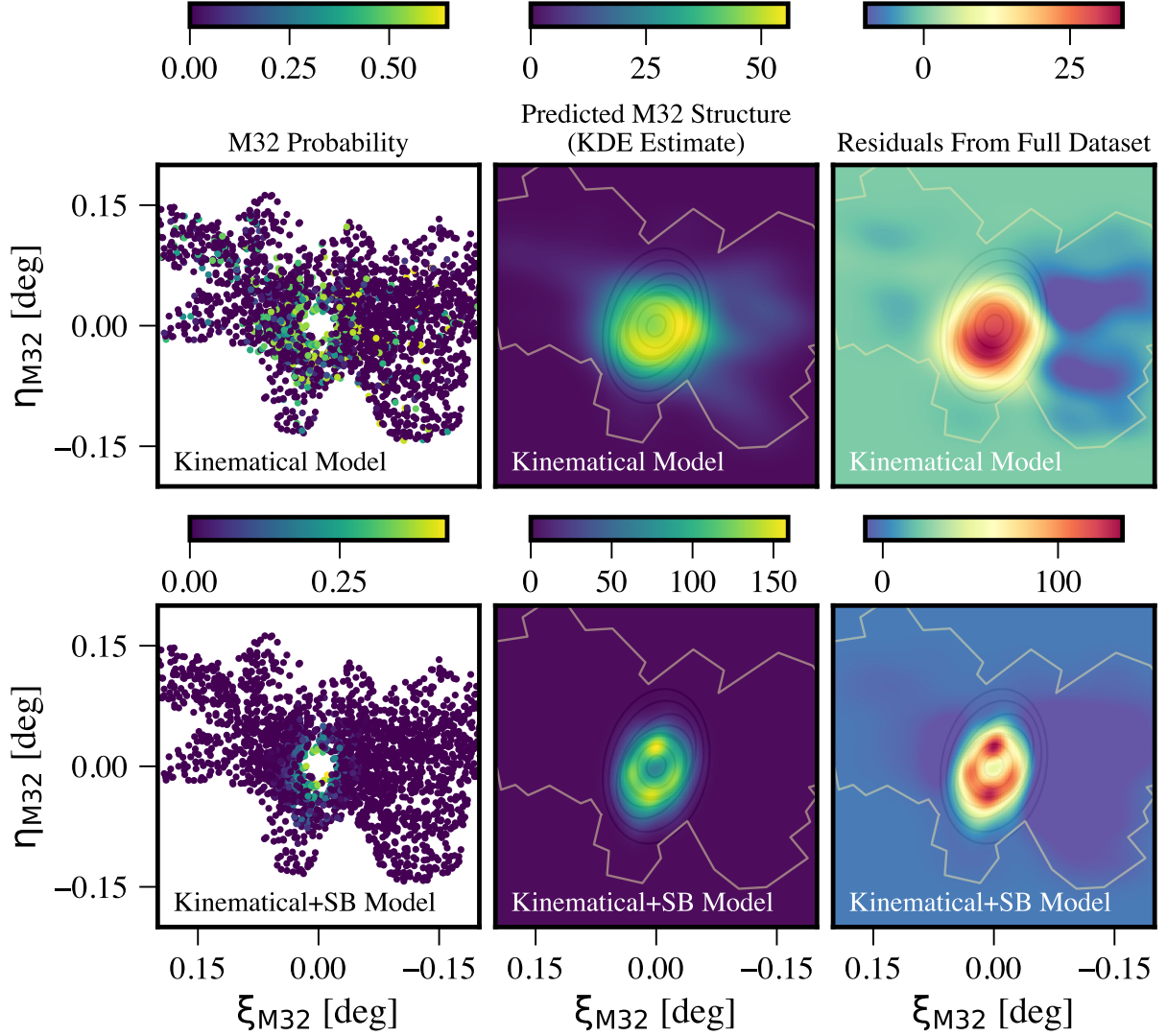


Figure 11. (Left panels) Location of M31/M32 giant stars in our dataset on the sky, color-coded by probability of M32 association based on their spatial positions and velocities predicted from kinematical modeling (Section 4.2). We show predictions from $p_{M32,vel}$ (top panels; Equation 10) and $p_{M32,vel} \times p_{M32,SB}$ (bottom panels; Section 2.1). The net effect of incorporating $p_{M32,SB}$ is decreasing p_{M32} overall, particularly at large M32-centric radii. (Middle panels) Relative 2D probability density of M32 on the sky constructed from a Gaussian kernel density estimate weighted according to probability of belonging to M32 and the inverse square of the velocity measurement uncertainty. I-band isophotes for M32 are overlaid, with R_{iso} bolded (black ellipses; C02). We also show the data footprint from Figure 1 for reference (yellow outlines). (Right panels) Residuals between maps of M32 and similar maps created using all M31/M32 giant stars in the dataset (i.e. unweighted by p_{M32}). The residual maps based on kinematical models alone (top panels) show that M32 is more likely to be identified toward the southeast (away from M31), with tentative evidence of structure beyond the outermost isophote. The maps incorporating surface-brightness information (bottom panels) show density enhancements near the isophotal twisting radius ($R_{iso} \sim 5r_{eff} \sim 150''$ or 0.56 kpc).

surface-brightness information ($p_{M32,vel} \times p_{M32,SB}$). The net effect of incorporating $p_{M32,SB}$ is to decrease the total M32 probability, particularly at large M32-centric radii, thereby increasing PDF amplitudes near M32's center. However, as discussed in Section 5.1, the predicted M32 fractions from 2D surface-brightness profiles tend to be systematically lower at a given radius than those from the line-of-sight velocity distribution

(H13). In the maps highlighting the predicted structure in M32's inner regions, the most notable features to emerge are the density enhancements located along M32's major axis and near R_{iso} . These density enhancements do not correspond to highly sampled regions in the data (e.g., the HST/ACS PM field; Figure 1) and neither do they appear in 2D PDFs that we constructed from weighting by $p_{M32,SB}$ alone as a test of whether

these features are intrinsic to the surface brightness profile and the data footprint.

6. SUMMARY & DISCUSSION

Based on a sample of 2525 individual giant stars with radial velocities from Keck/DEIMOS spectroscopy along the line-of-sight to M32, we have modeled M32’s kinematics between 0.9–15.5 arcmin from its center. Motivated by the methodology presented in Gilbert et al. 2022 and Cullinane et al. 2023, we have developed a framework to model the full line-of-sight velocity distribution as the combination of M31’s rotating stellar disk, which is anchored to its HI rotation curve (Chemin et al. 2009), and non-rotating components systematically offset from M31’s disk, which correspond to M32, a high-velocity dispersion population representing M31’s stellar halo, and any additional substructure that may be present in M31. In contrast to the only prior resolved kinematical study of M32 (H13), this novel approach enables spatially continuous modeling of the full survey area in a Bayesian context to directly address the complication of M32’s projected location at the edge of M31’s disk. Given our expanded sample size ($\sim 3.5\times$ larger usable unique target velocities) and spatial coverage (out to $\sim 23r_{\text{eff}}$ and $\sim 30r_{\text{eff}}$ along M32’s major and minor axes vs. $\sim 8r_{\text{eff}}$ for H13), this also allows us to revisit the kinematical evidence—or lack thereof—for signatures of tidal distortion in M32.

We analyzed the kinematics of M32 within and outside of the radius at which its I-band isophotes begin to twist and elongate ($R_{\text{iso}} \sim 150'' \sim 0.56$ kpc; C02) to search for any corresponding changes in M32’s velocity structure. Although the mean velocity and dispersion inside and outside R_{iso} are consistent, which is in agreement with H13, we find evidence for a change from negative to positive kurtosis ($\kappa_v \sim 0.15$ to ~ -0.3). This indicates that M32’s inner velocity distribution is relatively flat with few outliers, which may be due to its ordered rotation, whereas M32’s outer velocity distribution is more sharply peaked with heavy outliers (Figure 9). These outliers may exceed M32’s escape velocity ($v_{\text{M32}} \pm 72$ km s $^{-1}$; H13). Indeed, we find evidence for stars associated with M32 beyond its tidal radius ($R_{\text{tidal}} \sim 1.2$ kpc; C02), where stars at M32-like velocities are present even when surface brightness information alone predicts the contribution from M32 should be negligible (Figure 5). If these stars are bound to M32, we interpret them as evidence for either a dark matter halo or non-equilibrium tidal distortions in M32’s outskirts (see H13 and Section 5.1). We deem the third possible explanation of these stars belonging to unknown M31 substructure to be less likely, given that we have explicitly included com-

ponents to account for this possibility in our kinematical model (Section 4.2.1).

In addition to investigating M32’s observed line-of-sight velocity distribution, we modeled M32’s rotation with respect to R_{iso} , with the rotational axis as a free parameter (Section 5.2). We recover a weak rotational signature along M32’s major axis within R_{iso} ($k_R \sim 7$ km s $^{-1}$, $\theta_R \sim -30$ deg E of N), in accordance with expectations from H13. Interestingly, we find evidence of a shift in M32’s rotational direction beyond R_{iso} to approximately along M32’s minor axis ($k_R \sim 5$ km s $^{-1}$, $\theta_R \sim -130$ deg E of N; Figure 10), acknowledging that line-of-sight rotational signatures can be equivalently modeled as linear velocity gradients. In maps of M32’s structure on the sky predicted by our kinematical model (Figure 11), we similarly find hints of structural elongations in M32’s minor-axis direction (Section 5.3). Based on the expected rotational pattern of M31’s stellar disk (Figure 6; Section 4.1), it is unlikely that these features are caused by M31 contamination.

Taken together with the change in M32’s velocity distribution with respect to R_{iso} and the presence of stars with M32-like velocities at large M32-centric radii (Section 5.1), we argue that this presents compelling evidence that M32’s stellar outskirts have been tidally distorted by interactions with M31.⁹ Although prior observational constraints from H13 and C02 provided minimal apparent support for tidal distortions, this conclusion was largely limited to M32’s central ~ 1 kpc ($\lesssim 8r_{\text{eff}}$ or $\lesssim 1.5R_{\text{iso}}$). In contrast, our detection of distinct M32 kinematics beyond R_{iso} is based on a larger radial range ($\gtrsim 3R_{\text{M32}}$, or $\lesssim 6R_{\text{iso}}$). If M32’s progenitor had an intrinsically compact and dense core, it is reasonable to expect little tidal evolution in its central regions (see discussion by D’Souza & Bell 2018). Yet the existence of tidal distortions in the outskirts of M32 does not provide decisive evidence in favor of M32 being the remnant of a tidally stripped disk progenitor (e.g., Bekki et al. 2001), given that modest amounts of stripping are still expected in scenarios where M32’s progenitor is a dwarf galaxy of similar present-day stellar mass (Dierickx et al. 2014, see also Du et al. 2019).

Detailed kinematics for cEs near massive hosts beyond the Local Group could place M32 in context toward informing its most likely formation pathway. However,

⁹ Alternately, M32’s outskirts may have contributions from a “fossil” disk component as purported by Graham 2002, which could be supported by the change in M32’s rotational pattern (Section 5.2). In this case, the progenitor would have still experienced tidal stripping by M31. Interactions with other M31 dwarf galaxies may also contribute to tidal distortions in M32.

owing to the lack of nearby cEs that can be resolved into individual stars, kinematical information for cEs in the local universe is limited to coarse rotational and velocity dispersion profiles from integrated light spectroscopy (e.g., Ferré-Mateu et al. 2021). Although not classified as a cE, the nearby dwarf elliptical satellite galaxy of M31, NGC 205, provides a comparison system to M32 owing to its similarly elliptical morphology and observed twisting of isophotes in its surface brightness profile (C02). Based on the abrupt turnover in the major axis velocity profile at the isophotal twisting radius (Geha et al. 2006), NGC 205 has likely experienced a strong tidal interaction with M31 in the past (e.g., Howley et al. 2008). In particular, the orientation of NGC 205’s major-axis rotation flips beyond this radius, where the stellar motion in NGC 205’s outskirts implies it is on a prograde encounter with M31 (Geha et al. 2006). In comparison to NGC 205, H13 concluded that M32’s kinematics appeared symmetric across M32’s major axis, without clear gradients across M32’s region of isophotal elongation. However, the shift in M32’s rotational direction beyond its isophotal twisting radius (Section 5.2) could imply that similar physical mechanisms are at play in M32 and NGC 205. If these mechanisms are tidal in origin, they may depend on the intrinsic rotational properties and orbit of each galaxy.

The current sample of existing models for tidal encounters between M32 and M31 provides limited insight in terms of expected kinematical effects on M32. C02, who focused on purely photometric indicators, argued that the detection of twisted isophotes in M32 indicated an inclined orbital plane relative to M32’s direction of motion ($i \lesssim 70^\circ$). Furthermore, they inferred that the location of the breaks in the surface brightness profile implies a highly eccentric orbit with M32 currently near apocenter (± 10 kpc relative to M31) based on comparisons to simulations of satellites (Johnston et al. 2002). If these inferred orbital properties are accurate, the orientation of M32’s isophote at the break (PA ~ -25 deg E of N at $R_{\text{iso}} \sim 0.56$ kpc) should be pointed away from M32’s direction of motion, or clockwise around M31 (PA ~ 65 deg E of N; C02). The sense of this inferred orbit may be naively consistent with our detection of a change in M32’s rotational direction to being tentatively oriented along M32’s minor axes ($\theta_{R,\text{outer}} \sim -130$ deg E of N; Figure 10) and M32’s apparent structural elongation in this direction (Figure 11). It is unclear how exactly the orbit for M32 deduced by C02 relates to those in models focused on passages of M32 through M31’s disk to perturb M31’s disk velocity structure and star formation history (Gordon et al. 2006; Block et al. 2006;

Dierickx et al. 2014), with simulated orbits ranging from polar to nearly radial orientations.

Modern self-consistent N-body models of the M31-M32 interaction using the most recent phase space constraints are therefore required to determine probable orbits for M32 and whether the observed kinematical signatures presented in this work (Section 5) agree with predictions for tidal distortion and/or stripping. For example, improved distances to M32 ($D_\odot \sim 772.7_{-22}^{+21}$ kpc; Savino et al. 2022) place the results of Dierickx et al. 2014 well outside the original 2σ confidence intervals for reproducing M32’s phase space coordinates. Although the uncertainties on M31’s bulk transverse motion remain significant (van der Marel & Guhathakurta 2008; Sohn et al. 2012; van der Marel et al. 2012), the impact of assuming *Gaia* proper motions (van der Marel et al. 2019; Salomon et al. 2021) should be considered in new M31-M32 interaction models. In conjunction with these factors, upcoming HST-based proper motions for M32 and accompanying orbital models (Fardal et al., in preparation; Patel et al., in preparation) will provide a crucial piece of evidence regarding whether M32 is indeed inconsistent with sharing the same progenitor as the GSS and its associated tidal shells (Fardal et al. 2013; Escala et al. 2022).

In addition to providing kinematical constraints for more sophisticated modeling of the interaction between M32 and M31, we anticipate that the outer velocity structure for M32 presented in this work will enable updated models of M32’s dynamical mass, as well as revisiting the tentative evidence for a dark matter halo in M32 (H13). The methodology for kinematically separating M32 from stellar populations in M31 detailed here (following Gilbert et al. 2022 and Cullinane et al. 2023) will also be useful for disentangling M32’s resolved stellar chemical abundance distribution from M31. This will shed further light on formation scenarios for M32, particularly in comparison to existing chemical abundance measurements in M31’s inner stellar halo and tidal substructures (Gilbert et al. 2019; Escala et al. 2019, 2020a,b, 2021; Wojno et al. 2023). Finally, the methodology could also be applied across M31’s disk to provide a high-fidelity separation from M31’s rotating inner halo (c.f. Dorman et al. 2012; Escala et al. 2023) toward exploring the disk-halo connection in M31 and implications for the merger history of the M31 system.

1 The authors thank Ekta Patel and Roeland van der
 2 Marel for insightful discussions on M32’s orbit and mass
 3 modeling, David W. Hogg for useful discussions on sta-
 4 tistical modeling, Charis Tsakonas, Magda Arnaboldi,
 5 and François Hammer for enlightening conversations on
 6 the role of M32 in a major merger scenario, and Anil
 7 Seth for contributions to the slitmask design. We also
 8 thank interns David Carter Oropeza, Ali Behram Gu-
 9 mus, Derek Maeshiro, and Adrian Torres from the Sci-
 10 ence Internship Program (SIP) at the University of Cal-
 11 ifornia, Santa Cruz, for assisting with velocity measure-
 12 ments.

13 IE acknowledges financial support from programs
 14 HST GO-15891, GO16235, and GO-16786, provided by
 15 NASA through a grant from the Space Telescope Science
 16 Institute, which is operated by the Association of Uni-
 17 versities for Research in Astronomy, Inc., under NASA
 18 contract NAS 5-26555, and from a Carnegie-Princeton
 19 Fellowship through Princeton University.

20 We are grateful to the many people who have worked
 21 to make the Keck Telescope and its instruments a re-
 22 ality and to operate and maintain the Keck Observa-
 23 tory. The authors wish to recognize and acknowledge
 24 the very significant cultural role and reverence that the
 25 summit of Maunakea has always had within the indige-
 26 nous Hawaiian community. We are most fortunate to
 27 have the opportunity to conduct observations from this
 28 mountain.

Facilities: HST(ACS,WFPC2), Keck(DEIMOS),
 CFHT(MegaCam)

Software: astropy, dynesty, numpy, scipy, matplotlib

APPENDIX

A. ALTERNATE KINEMATICAL MODELS

A.1. Models Assuming Uniform Priors

Here, we provide technical details on the “rotating plus offset” velocity models (Section 4.2) assuming uniform priors on all parameters discussed in Section 4.2.1. In the dynamic nested sampling implementation using DYNESTY (Speagle 2020), we allowed f_{rot} to vary between 0 and 1.5, bounded f_v between 0 and 1, μ_v between -800 and $+200$ km s^{-1} , and assumed an upper limit on σ_v of 250 km s^{-1} . We also adopted the following constraints: $\Sigma_N f_v^N = 1$, $\sigma_{v,\text{disk}} < \sigma_{v,\text{halo}}$, and 5 $\text{km s}^{-1} < \sigma_{v,N} < \sigma_{v,\text{disk}}$, and $\mu_v^N < \mu_v^{N-1}$ to prevent degeneracy between model components in the sampling procedure. We sampled all models over *identical* prior volumes, regardless of whether all parameters were used in the evaluation of a given likelihood function, to enable comparisons of the Bayesian evidence (\mathcal{Z}). Table A.1 summarizes the various N -component models, including the change in the evidence estimation for each additional offset component, $\Delta \log \mathcal{Z} = \log \mathcal{Z}_N - \log \mathcal{Z}_{N-1}$. We increased the number of model components until $\Delta \log \mathcal{Z}$ became negative, which indicates that N components is not preferred over $N - 1$ components based on the Bayes factor thresholds for interpreting model evidence by Kass & Raftery (1995) (see also Table 2 of Cullinane et al.

Table 4. Kinematical Parameters for Rotating Plus Offset Model – Uniform Priors

Model	f_{rot}	σ_{disk} [km s $^{-1}$]	Comp.	f_v	μ_v [km s $^{-1}$]	σ_v [km s $^{-1}$]	$\log \mathcal{Z}_N - \log \mathcal{Z}_{N-1}$
	Disk		Offset Components				
	All Stars						
2D	$0.79^{+0.02}_{-0.04}$	$123.4^{+1.4}_{-3.0}$	First	$0.11^{+0.01}_{-0.03}$	$-185.4^{+10.8}_{-30.1}$	$130.3^{+4.5}_{-6.5}$	+12.7
3D	$0.88^{+0.02}_{-0.04}$	$114.3^{+2.9}_{-7.5}$	First	$0.18^{+0.04}_{-0.07}$	$-276.6^{+33.7}_{-31.5}$	$172.8^{+5.6}_{-26.0}$	+12.4
			Second	$0.06^{+0.01}_{-0.01}$	$-186.0^{+2.0}_{-4.3}$	$23.7^{+2.3}_{-4.6}$	
4D	$0.81^{+0.02}_{-0.04}$	$106.3^{+2.5}_{-5.7}$	First	$0.08^{+0.02}_{-0.04}$	$-498.7^{+17.0}_{-35.1}$	$116.6^{+5.7}_{-10.0}$	+6.1
			Second	$0.08^{+0.01}_{-0.02}$	$-186.8^{+2.0}_{-4.4}$	$29.2^{+3.0}_{-5.5}$	
			Third	$0.06^{+0.01}_{-0.02}$	$-85.2^{+11.5}_{-25.5}$	$89.1^{+4.5}_{-11.7}$	
5D	$0.82^{+0.02}_{-0.04}$	$106.2^{+2.7}_{-6.1}$	First	$0.08^{+0.02}_{-0.04}$	$-490.9^{+18.2}_{-39.2}$	$120.5^{+7.5}_{-12.7}$	-4.4
			Second	$0.06^{+0.02}_{-0.04}$	$-248.4^{+57.6}_{-164.4}$	$32.8^{+13.0}_{-10.4}$	
			Third	$0.06^{+0.01}_{-0.04}$	$-180.8^{+36.9}_{-9.1}$	$36.2^{+16.5}_{-11.0}$	
			Fourth	$0.05^{+0.01}_{-0.03}$	$-72.0^{+20.7}_{-34.6}$	$85.0^{+5.9}_{-20.1}$	
Disk Region, $p_{\text{M32,SB}} < 0.01$							
2D	$0.97^{+0.02}_{-0.04}$	$90.6^{+2.9}_{-6.8}$	First	$0.37^{+0.03}_{-0.07}$	$-339.5^{+6.5}_{-13.2}$	$177.1^{+4.0}_{-8.0}$	+37.7
3D	$0.87^{+0.04}_{-0.07}$	$97.7^{+2.6}_{-6.6}$	First	$0.28^{+0.05}_{-0.09}$	$-425.8^{+17.1}_{-43.5}$	$128.0^{+7.8}_{-15.3}$	+3.1
			Second	$0.07^{+0.01}_{-0.02}$	$-87.2^{+12.5}_{-22.6}$	$89.0^{+3.5}_{-11.7}$	
4D	$0.86^{+0.03}_{-0.07}$	$93.6^{+3.0}_{-7.2}$	First	$0.26^{+0.04}_{-0.09}$	$-447.2^{+17.0}_{-44.3}$	$120.0^{+6.6}_{-13.9}$	-1.2
			Second	$0.05^{+0.01}_{-0.03}$	$-168.5^{+11.7}_{-39.0}$	$58.3^{+13.1}_{-23.3}$	
			Third	$0.04^{+0.01}_{-0.02}$	$-29.6^{+19.1}_{-51.2}$	$71.6^{+8.8}_{-21.2}$	
M32 Region, $p_{\text{M32,SB}} > 0.01$							
2D	$1.44^{+0.02}_{-0.08}$	$99.0^{+2.6}_{-5.3}$	First	$0.56^{+0.02}_{-0.04}$	$-232.3^{+4.6}_{-12.7}$	$101.4^{+2.8}_{-5.6}$	+1.4
3D	$1.15^{+0.05}_{-0.11}$	$51.2^{+7.3}_{-12.3}$	First	$0.61^{+0.04}_{-0.13}$	$-335.3^{+4.3}_{-9.7}$	$149.4^{+3.5}_{-6.5}$	+37.1
			Second	$0.22^{+0.02}_{-0.04}$	$-195.1^{+1.9}_{-4.3}$	$35.3^{+2.3}_{-5.2}$	
4D	$1.16^{+0.06}_{-0.13}$	$49.0^{+8.4}_{-12.4}$	First	$0.62^{+0.04}_{-0.17}$	$-338.1^{+4.3}_{-11.3}$	$147.1^{+3.5}_{-6.9}$	-2.2
			Second	$0.18^{+0.02}_{-0.09}$	$-198.1^{+2.5}_{-8.7}$	$32.7^{+2.8}_{-6.5}$	
			Third	$0.03^{+0.03}_{-0.03}$	$-154.2^{+33.4}_{-35.8}$	$34.3^{+6.1}_{-13.8}$	

2023). For models with positive $\Delta \log \mathcal{Z}$, we considered the N -component model a better description of the data if there was “positive/substantial” evidence in favor of this hypothesis when compared to the $N - 1$ component model ($\Delta \log \mathcal{Z} \geq 0.5$). We find “decisive” evidence ($\Delta \log \mathcal{Z} \geq 2.2$) preferring 4D, 3D, and 3D models for all M31/M32 giant stars, stars in the “Disk Region” ($p_{\text{M32,SB}} < 0.01$), and stars in the “M32 Region” ($p_{\text{M32,SB}} > 0.01$) respectively. We discuss the physical interpretation of these model components in Section 4.2.1, where Figure 12 shows the best-fit velocity models assuming uniform priors (Table A.1) for each spatial sample.

A.2. Models with Multiple Rotating Components

In this section, we evaluate whether models with multiple rotating components, such as a two-component disk and/or a rotating stellar halo, could provide a better description of the observed velocity distribution than the fiducial model composed of a single rotating disk component and an offset stellar halo (Section 4.2). The high velocity dispersion in the case of a single disk component (Table 3), as well as the apparent asymmetry near the disk velocity peak extending toward more negative velocities (Figure 8), provides reason to explore the possibility of a two-component disk structure. Moreover, Dorman et al. (2012) found signatures of rotation in M31’s stellar halo, with $V_{\text{rot,halo}} = 52.6 \pm 6.8$ km s $^{-1}$ for $R_{\text{proj}} > 5$ kpc approximately from M31’s southwest to northeast major axis (the same direction as M31’s disk rotation). Assuming that M31’s halo rotates in the plane of the disk with $V_{\text{rot,halo,max}} = 52.6$ km s $^{-1}$, its predicted median line-of-sight velocity is $v_{\text{los,halo}} = -317.7 \pm 9.6$ km s $^{-1}$ over the DEIMOS footprint (from an analogous modification of Equation 8), where $v_{\text{los,halo}}$ has predicted maximum and minimum values of -303 and -348 km s $^{-1}$ over this area.

To implement multiple rotating components, we modified the likelihood function in Equation 10 accordingly and sampled the posterior distribution using DYNesty (Speagle 2020). For a two-component disk structure, we assumed kinematically “thinner” and “thicker” disks, following the constraints $\sigma_{v,\text{thin}} < \sigma_{v,\text{thick}}$ and $f_{\text{rot,thin}} > f_{\text{rot,thick}}$. Given

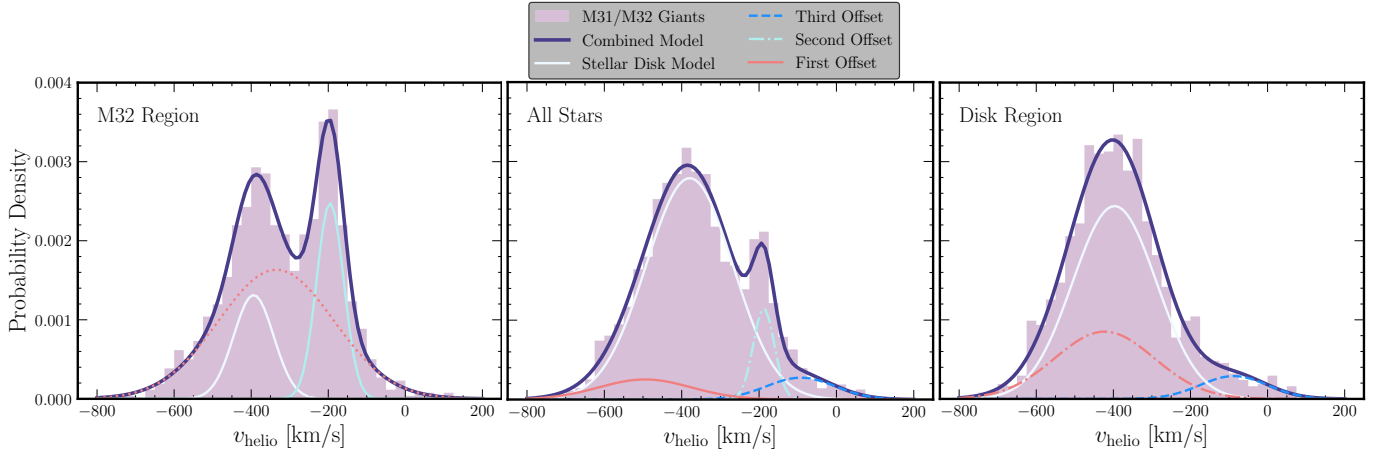


Figure 12. Same as Figure 8, except assuming uniform priors agnostic of the physical nature of the “offset” components for the best-fit velocity models (Appendix A.1). We find evidence for a kinematically cold component corresponding to M32 and two kinematically hot components with mean velocities shifted toward the negative and positive extrema of the velocity distributions. This motivates our fiducial assumption of four total offset components when considering our prior physical knowledge of the system, where we interpret the two kinematically hot components as a M31 halo-like component plus two kinematically colder components at the positive (MW-like) and negative (GSS-like) velocity tails of the distribution (Section 4.2.1, 4.2.2).

that the MW-like and GSS-like model components combined contribute $\sim 4\%$ of the total stellar population (Table 3), we omitted these features in this modeling exercise for simplicity, considering models composed only of M32, M31’s stellar halo, and M31’s stellar disk(s). We enforced normal priors on M32 and M31’s halo velocity dispersion (Table 4.2.2), but lifted the normal priors on M31’s disk velocity dispersion, instead requiring that $\sigma_{v,\text{thick}} < \sigma_{v,\text{halo}}$ in addition to the aforementioned constraints on the disk(s). In the case of a non-rotating “offset” halo, we imposed normal priors on $\mu_{v,\text{halo}}$ (Table 4.2.2). For a rotating halo, we adopted the constraints $f_{\text{rot,halo}} < f_{\text{rot,thick}}$ in the case of a two-component disk structure and $f_{\text{rot,halo}} < f_{\text{rot,disk}}$ otherwise. We also implemented the Gaussian prior $\mathcal{N}(0.2|0.05)$ on $f_{\text{rot,halo}}$ based on the predicted values of $V_{\text{rot,halo}}/V_{\text{HI,rot}}$ over the DEIMOS footprint, and retained the prior on f_{halo} (Table 4.2.2) for both rotating and non-rotating halo models. We estimated the Bayesian evidence \mathcal{Z} over this fixed prior volume for *all* model parameters (i.e., for a two-component disk, rotating halo, and non-rotating halo) and resampled the posterior distribution of the standard 3D model (Table 3) under these prior assumptions.

We found that, under the assumption of an offset halo, a two-component disk is decisively preferred ($\Delta \log \mathcal{Z} \sim 5.4$). Interestingly, there is no statistically significant difference between a model composed of a single-component disk and a rotating halo versus a model with a two-component disk and an offset halo, implying that the secondary rotating component in each model may describe similar features in the data. Under the assumption of a rotating halo, a two-component disk model is also decisively preferred ($\Delta \log \mathcal{Z} \sim 6.4$). In this model, $\sigma_{v,\text{thin}} \sim 30 \text{ km s}^{-1}$ and $\sigma_{v,\text{thick}} \sim 110 \text{ km s}^{-1}$ with $f_{\text{rot,thin}} \sim 1.1$ and $f_{\text{rot,thick}} \sim 0.95$ for the “thin” and “thick” disk components, where $f_{\text{rot,halo}} \sim 0.24$ and $\sigma_{v,\text{halo}} \sim 155 \text{ km s}^{-1}$ for the rotating halo. Thus, the addition of a “thin” disk does not reduce the velocity dispersion of the “thick” disk, nor does it account for the negative tail of the observed velocity distribution.

Given that M31’s disk and halo components effectively provide nuisance parameters over which we marginalize to extract M32’s line-of-sight velocity distribution, we assumed a model composed of a single-component disk and offset halo in this work for simplicity. The computed M32 probabilities for a given star (Equation 10) are strongly correlated under each of the four models explored here, and therefore do not significantly alter our main results regarding M32 (Section 5). A more detailed analysis over a larger and more representative area of M31’s southern disk region, free of the added complexity of M32, is required to confirm whether its velocity distribution supports a rotating halo or a multiple-component disk structure and is therefore beyond the scope of this paper.

A.3. Models with Stellar Age

In Section 4, we modeled the kinematics of the entire sample of M31/M32 giant stars (regardless of stellar classification) in order to maximize our sample size and spatial coverage, assuming that the hotter kinematics of the older RGB population encompasses that of the kinematically colder and younger AGB stars. To explore kinematical differences with respect to stellar age, we separated our spectroscopic sample into RGB and AGB populations (Section 3.2), then

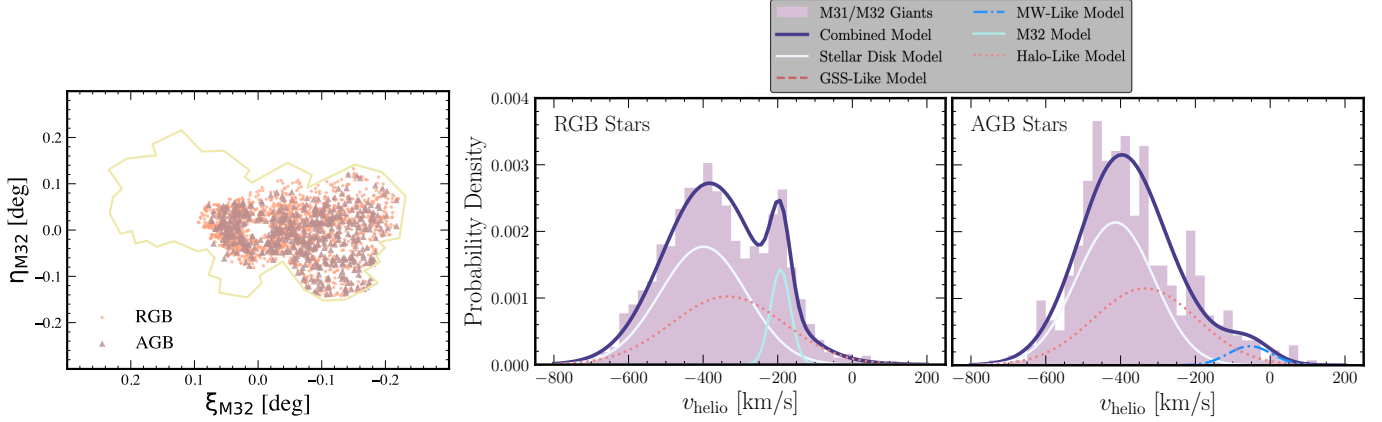


Figure 13. (Left) M32-centric sky location of RGB (orange points) and AGB (brown triangles; Section 3.2) stars, whose classification is limited to the PHAST footprint (compared to the DEIMOS footprint in Figure 1; yellow outline). (Right panels) Similar to Figure 8, except for the RGB and AGB star velocity distributions (Section A.3). M32 is primarily traced by the old RGB population, where a statistically significant M32 contribution is not detected in the AGB stars despite the visible peak at -200 km s^{-1} . More AGB than RGB stars are present at MW-like velocities. Neither the RGB nor AGB stars favor a significant GSS-like component despite the peaks of stars at -600 km s^{-1} . We find that the kinematical parameters describing each component between the RGB, AGB, and fiducial models (Tables 3 and 5) are in broad agreement.

Table 5. Kinematical Parameters for Rotating Plus Offset Models by Stellar Type – Normal Priors

Model	f_{rot}	$\sigma_{\text{disk}} [\text{km s}^{-1}]$	Comp.	f_v	$\mu_v [\text{km s}^{-1}]$	$\sigma_v [\text{km s}^{-1}]$
	Disk		Offset Components			
	RGB Stars					
3D	$0.94^{+0.03}_{-0.06}$	$110.2^{+2.8}_{-6.4}$	Halo-Like	$0.39^{+0.02}_{-0.05}$	$-334.7^{+3.5}_{-8.1}$	$151.2^{+2.3}_{-5.3}$
			M32	$0.10^{+0.01}_{-0.02}$	$-192.7^{+1.4}_{-3.2}$	$27.2^{+1.6}_{-3.7}$
	AGB Stars					
3D	$1.03^{+0.03}_{-0.08}$	$96.6^{+3.4}_{-7.3}$	Halo-Like	$0.41^{+0.02}_{-0.05}$	$-334.2^{+4.3}_{-10.8}$	$139.8^{+4.1}_{-9.8}$
			MW-Like	$0.04^{+0.01}_{-0.02}$	$-55.3^{+4.1}_{-9.7}$	$56.1^{+3.8}_{-10.6}$

repeated the kinematical modeling procedure for the RGB and AGB samples. We also modeled the combined RGB and AGB sample (i.e., all stars with stellar classifications as opposed to the full sample of all M31/M32 giant stars) to control for the areal coverage of this subsample, which traces the PHAST survey area. We found results fully consistent with Table 3, which indicates that any resulting kinematical differences between the RGB and AGB stars are not driven by the PHAST versus DEIMOS footprints. We show the RGB and AGB velocity distributions, as well as their spatial distributions, in Figure 13. The RGB velocities show clear peaks associated with M31’s stellar disk and M32, and a negatively skewed asymmetry in the disk velocity peak that may suggest the presence of stars at GSS-like velocities or possibly multiple disk components (Section A.2). The AGB velocity distribution appears dominated by M31’s stellar disk, with small peaks at -600 and -200 km s^{-1} and a more prominent tail toward MW-like velocities.

For the RGB stars, we found evidence for M31’s stellar disk and two offset model components corresponding to M32 and a kinematically hot component with halo-like dispersion ($\sigma_v \sim 155 \text{ km s}^{-1}$) but mean velocity shifted toward the positive tail of the distribution ($\mu_v \sim -220 \text{ km s}^{-1}$). We thus initially assumed an RGB model with four total components: M31’s stellar disk, an M31 halo-like component, M32, and a MW-like component. For the AGB stars, we found evidence for M31’s stellar disk and a single offset component with high velocity dispersion ($\sigma_v \sim 120 \text{ km s}^{-1}$) and relatively positive mean velocity ($\mu_v \sim -140 \text{ km s}^{-1}$). We thus assumed a three component AGB model consisting of M31’s stellar disk, an M31-halo like population, and a MW-like population. Despite the presence of a small peak at velocities characteristic of M32 (Figure 13), the AGB distribution does not support a significant M32 contribution, suggesting that our spectroscopic sample predominately traces the old RGB population in M32 (Section 3.2).

When assuming the normal priors from Table 4.2.2, including the constraints on the fractional halo-like contribution f_h , the best-fit RGB model supports three components: M31’s stellar disk, M32, and an M31 halo-like component.

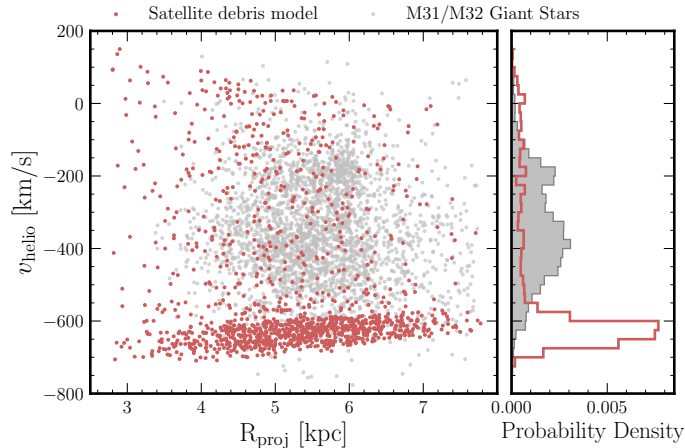


Figure 14. Heliocentric velocity versus projected M31-centric radius over the DEIMOS footprint (Figure 1) for M31/M32 giant stars (silver points; Section 3.1) and satellite debris particles from an N-body model for the formation of the GSS in a minor merger (red points; Fardal et al. 2012; Escala et al. 2022; Section 4.2.2). Observational velocity errors are not shown for clarity (median 4.2 km s^{-1}). The model predicts M31 to dominate the stars in this region, though GSS-related tidal debris should be most detectable near -600 km s^{-1} (Table 4.2.2). The predicted debris also extends to MW-like velocities (near 0 km s^{-1}).

This differs from the four components inferred from uniform priors, likely because the comparatively small number of RGB stars at the MW-like tail of the velocity distribution are subsumed into the high-dispersion halo. We confirmed that including a MW-like component ($\Delta \log \mathcal{Z} \sim -2.8$) or GSS-like component ($\Delta \log \mathcal{Z} \sim -0.45$) is not preferred for the RGB velocity distribution. In the case of normal priors, the AGB velocity distribution is still best described by the 3D model including the MW-like component, as opposed to a simpler model consisting solely of M31’s stellar disk and halo ($\Delta \log \mathcal{Z} \sim -1.9$). We verified that including an M32 component either instead of ($\Delta \log \mathcal{Z} \sim -3.8$) or in addition to ($\Delta \log \mathcal{Z} \sim -1.7$) the MW-like component is not preferred. Similarly, adding a GSS-like component to the standard 3D AGB model is also disfavored ($\Delta \log \mathcal{Z} \sim -5.3$).

Table 5 summarizes the kinematical parameters for the adopted RGB and AGB models (Figure 13). The RGB and AGB stars rotate with similar speeds as the HI gas, where the RGB stars may slightly lag the HI disk ($f_{\text{rot}} \sim -0.9$) in addition to having a marginally larger dispersion ($\sigma_v \sim 110 \text{ km s}^{-1}$) compared to the AGB stars. Moreover, the dispersion of the M31 halo-like component may be higher for the RGB stars than the AGB stars. Despite these minor differences, the RGB and AGB velocity distributions do not differ substantially over our survey area, supporting our choice to model the entire M31/M32 giant distribution in Section 4.

Compared to the adopted 5D model for all M31/M32 giant stars (Table 3), M31’s disk dispersion is higher for the RGB model by $\sim 2.6\sigma$. This may be driven by an intrinsically higher disk dispersion compared to a sample containing AGB stars and/or the putative GSS-like population being subsumed into the rotating model component in the absence of a dedicated GSS-like component in the adopted RGB model, thereby inflating the modeled disk dispersion. The dispersion of the M31 halo-like components are in broad agreement, where the AGB halo dispersion is marginally lower by $\sim 1.3\sigma$ compared to the halo-like component in the fiducial 5D model. Otherwise, the kinematical parameters describing the M32 and MW-like components are in good agreement.

We defer further modeling and analysis of kinematical differences between RGB and AGB populations in M32, M31’s stellar disk, M31’s stellar halo, and possible M31 substructure to future work, ideally based on spectroscopic samples with more comprehensive spatial coverage of M31’s southern disk region (Grion Filho et al., in preparation) and with larger samples of giant stars with available PHAST photometry.

B. PREDICTIONS FOR GSS MERGER-RELATED TIDAL DEBRIS

Here, we present Figure 14 demonstrating predictions for satellite tidal debris from the GSS progenitor in a minor merger scenario (Fardal et al. 2012; Escala et al. 2022), which we use to inform our prior selection in Section 4.2.2.

REFERENCES

- Beaton, R. L., Freedman, W. L., Madore, B. F., et al. 2016, *ApJ*, 832, 210. doi:10.3847/0004-637X/832/2/210
- Bekki, K., Couch, W. J., Drinkwater, M. J., et al. 2001, *ApJL*, 557, L39. doi:10.1086/323075

- Bender, R., Kormendy, J., & Dehnen, W. 1996, *ApJL*, 464, L123. doi:10.1086/310098
- Bernard, E. J., Ferguson, A. M. N., Richardson, J. C., et al. 2015, *MNRAS*, 446, 2789. doi:10.1093/mnras/stu2309
- Block, D. L., Bournaud, F., Combes, F., et al. 2006, *Nature*, 443, 832. doi:10.1038/nature05184
- Bian, Y., Du, M., Debattista, V. P., et al. 2024, arXiv:2409.05229. doi:10.48550/arXiv.2409.05229
- Bressan, A., Marigo, P., Girardi, L., et al. 2012, *MNRAS*, 427, 127. doi:10.1111/j.1365-2966.2012.21948.x
- Burkert, A. 1994, *MNRAS*, 266, 877. doi:10.1093/mnras/266.4.877
- Caldwell, N., Walker, M. G., Mateo, M., et al. 2017, *ApJ*, 839, 20. doi:10.3847/1538-4357/aa688e
- Caso, J. P., Vega Neme, L., De Bórtoli, B. J., et al. 2024, *A&A*, 691, A307. doi:10.1051/0004-6361/202452113
- Chen, Y., Bressan, A., Girardi, L., et al. 2015, *MNRAS*, 452, 1068. doi:10.1093/mnras/stv1281
- Chemin, L., Carignan, C., & Foster, T. 2009, *ApJ*, 705, 1395. doi:10.1088/0004-637X/705/2/1395
- Chilingarian, I., Cayatte, V., Chemin, L., et al. 2007, *A&A*, 466, L21. doi:10.1051/0004-6361:20077291
- Chilingarian, I., Cayatte, V., Revaz, Y., et al. 2009, *Science*, 326, 1379. doi:10.1126/science.1175930
- Chilingarian, I. & Zolotukhin, I. 2015, *Science*, 348, 418. doi:10.1126/science.aaa3344
- Choi, P. I., Guhathakurta, P., & Johnston, K. V. 2002, *AJ*, 124, 310. doi:10.1086/341041
- Coelho, P., Mendes de Oliveira, C., & Cid Fernandes, R. 2009, *MNRAS*, 396, 624. doi:10.1111/j.1365-2966.2009.14722.x
- Cooper, M. C., Griffith, R. L., Newman, J. A., et al. 2012, *MNRAS*, 419, 3018
- Cullinane, L. R., Gilbert, K. M., Guhathakurta, P., et al. 2023, *ApJ*, 958, 157. doi:10.3847/1538-4357/ad003b
- Cseresnjés, P., Crotts, A. P. S., de Jong, J. T. A., et al. 2005, *ApJL*, 633, L105. doi:10.1086/498501
- D'Souza, R. & Bell, E. F. 2018, *Nature Astronomy*, 2, 737. doi:10.1038/s41550-018-0533-x
- Dalcanton, J. J., Williams, B. F., Lang, D., et al. 2012, *ApJS*, 200, 18. doi:10.1088/0067-0049/200/2/18
- Dalcanton, J. J., Fouesneau, M., Hogg, D. W., et al. 2015, *ApJ*, 814, 3. doi:10.1088/0004-637X/814/1/3
- Deeley, S., Drinkwater, M. J., Sweet, S. M., et al. 2023, *MNRAS*, 525, 1192. doi:10.1093/mnras/stad2313
- Dierickx, M., Blecha, L., & Loeb, A. 2014, *ApJL*, 788, L38. doi:10.1088/2041-8205/788/2/L38
- Dolphin, A. E. 2000, *PASP*, 112, 1383. doi:10.1086/316630
- Dolphin, A. 2016, *Astrophysics Source Code Library*. ascl:1608.013
- Dorman, C. E., Guhathakurta, P., Fardal, M. A., et al. 2012, *ApJ*, 752, 147. doi:10.1088/0004-637X/752/2/147
- Dorman, C. E., Widrow, L. M., Guhathakurta, P., et al. 2013, *ApJ*, 779, 103.
- Dorman, C. E., Guhathakurta, P., Seth, A. C., et al. 2015, *ApJ*, 803, 24. doi:10.1088/0004-637X/803/1/24
- Davidge, T. J., McConnachie, A. W., Fardal, M. A., et al. 2012, *ApJ*, 751, 74. doi:10.1088/0004-637X/751/1/74
- Draine, B. T., Aniano, G., Krause, O., et al. 2014, *ApJ*, 780, 172. doi:10.1088/0004-637X/780/2/172
- Du, M., Debattista, V. P., Ho, L. C., et al. 2019, *ApJ*, 875, 58. doi:10.3847/1538-4357/ab0e0c
- Escala, I., Kirby, E. N., Gilbert, K. M., et al. 2019, *ApJ*, 878, 42. doi:10.3847/1538-4357/ab1eac
- Escala, I., Gilbert, K. M., Kirby, E. N., et al. 2020, *ApJ*, 889, 177. doi:10.3847/1538-4357/ab6659
- Escala, I., Kirby, E. N., Gilbert, K. M., et al. 2020, *ApJ*, 902, 51. doi:10.3847/1538-4357/abb474
- Escala, I., Gilbert, K. M., Wojno, J., et al. 2021, *AJ*, 162, 45. doi:10.3847/1538-3881/abfec4
- Escala, I., Gilbert, K. M., Fardal, M., et al. 2022, arXiv:2203.16675
- Escala, I., Quirk, A. C. N., Guhathakurta, P., et al. 2023, *AJ*, 165, 75. doi:10.3847/1538-3881/aca9cd
- Falco, E. E., Kurtz, M. J., Geller, M. J., et al. 1999, *PASP*, 111, 438. doi:10.1086/316343
- Fardal, M. A., Guhathakurta, P., Babul, A., et al. 2007, *MNRAS*, 380, 15. doi:10.1111/j.1365-2966.2007.11929.x
- Fardal, M. A., Guhathakurta, P., Gilbert, K. M., et al. 2012, *MNRAS*, 423, 3134. doi:10.1111/j.1365-2966.2012.21094.x
- Fardal, M. A., Weinberg, M. D., Babul, A., et al. 2013, *MNRAS*, 434, 2779. doi:10.1093/mnras/stt1121
- Ferré-Mateu, A., Forbes, D. A., Romanowsky, A. J., et al. 2018, *MNRAS*, 473, 1819. doi:10.1093/mnras/stx2442
- Ferré-Mateu, A., Durré, M., Forbes, D. A., et al. 2021, *MNRAS*, 503, 5455. doi:10.1093/mnras/stab805
- Fiorentino, G., Monachesi, A., Trager, S. C., et al. 2010, *ApJ*, 708, 817. doi:10.1088/0004-637X/708/1/817
- Fiorentino, G., Contreras Ramos, R., Tolstoy, E., et al. 2012, *A&A*, 539, A138. doi:10.1051/0004-6361/201117434
- Gallazzi, A., Charlot, S., Brinchmann, J., et al. 2005, *MNRAS*, 362, 41. doi:10.1111/j.1365-2966.2005.09321.x
- Geha, M., Guhathakurta, P., Rich, R. M., et al. 2006, *AJ*, 131, 332. doi:10.1086/498686
- Gilbert, K. M., Guhathakurta, P., Kalirai, J. S., et al. 2006, *ApJ*, 652, 1188. doi:10.1086/508643
- Gilbert, K. M., Fardal, M., Kalirai, J. S., et al. 2007, *ApJ*, 668, 245. doi:10.1086/521094

- Gilbert, K. M., Guhathakurta, P., Kollipara, P., et al. 2009, *ApJ*, 705, 1275. doi:10.1088/0004-637X/705/2/1275
- Gilbert, K. M., Guhathakurta, P., Beaton, R. L., et al. 2012, *ApJ*, 760, 76. doi:10.1088/0004-637X/760/1/76
- Gilbert, K. M., Tollerud, E., Beaton, R. L., et al. 2018, *ApJ*, 852, 128. doi:10.3847/1538-4357/aa9f26
- Gilbert, K. M., Kirby, E. N., Escala, I., et al. 2019, *ApJ*, 883, 128. doi:10.3847/1538-4357/ab3807
- Gilbert, K. M., Quirk, A. C. N., Guhathakurta, P., et al. 2022, *ApJ*, 924, 116. doi:10.3847/1538-4357/ac3480
- Gordon, K. D., Bailin, J., Engelbracht, C. W., et al. 2006, *ApJL*, 638, L87. doi:10.1086/501046
- Graham, A. W. 2002, *ApJL*, 568, L13. doi:10.1086/340274
- Gregersen, D., Seth, A. C., Williams, B. F., et al. 2015, *AJ*, 150, 189. doi:10.1088/0004-6256/150/6/189
- Guhathakurta, P., Ostheimer, J. C., Gilbert, K. M., et al. 2005, *astro-ph/0502366*. doi:10.48550/arXiv.astro-ph/0502366
- Guhathakurta, P., Rich, R. M., Reitzel, D. B., et al. 2006, *AJ*, 131, 2497. doi:10.1086/499562
- Hammer, F., Yang, Y. B., Wang, J. L., et al. 2010, *ApJ*, 725, 542. doi:10.1088/0004-637X/725/1/542
- Hammer, F., Yang, Y. B., Wang, J. L., et al. 2018, *MNRAS*, 475, 2754. doi:10.1093/mnras/stx3343
- Higson, E., Handley, W., Hobson, M. et al. Dynamic nested sampling: an improved algorithm for parameter estimation and evidence calculation. *Stat Comput* 29, 891–913 (2019). doi:10.1007/s11222-018-9844-0
- Howley, K. M., Geha, M., Guhathakurta, P., et al. 2008, *ApJ*, 683, 722. doi:10.1086/589632
- Howley, K. M., Guhathakurta, P., van der Marel, R., et al. 2013, *ApJ*, 765, 65. doi:10.1088/0004-637X/765/1/65
- Huxor, A. P., Phillipps, S., Price, J., et al. 2011, *MNRAS*, 414, 3557. doi:10.1111/j.1365-2966.2011.18655.x
- Huxor, A. P., Phillipps, S., & Price, J. 2013, *MNRAS*, 430, 1956. doi:10.1093/mnras/stt014
- Ibata, R., Irwin, M., Lewis, G., et al. 2001, *Nature*, 412, 49. doi:10.1038/35083506
- Jang, J. K., Yi, S. K., Rey, S.-C., et al. 2024, *ApJ*, 969, 59. doi:10.3847/1538-4357/ad4d8a
- Ji, A. P., Li, T. S., Hansen, T. T., et al. 2020, *AJ*, 160, 181. doi:10.3847/1538-3881/abacb6
- Johnston, K. V., Choi, P. I., & Guhathakurta, P. 2002, *AJ*, 124, 127. doi:10.1086/341040
- Jones, O. C., Boyer, M. L., McDonald, I., et al. 2023, *MNRAS*, 525, 3693. doi:10.1093/mnras/stad2472
- Joseph, C. L., Merritt, D., Olling, R., et al. 2001, *ApJ*, 550, 668. doi:10.1086/319781
- Kass, R. E., & Raftery, A. E. (1995). Bayes Factors. *Journal of the American Statistical Association*, 90(430), 773–795. doi:10.1080/01621459.1995.10476572
- Kirby, E. N., Cohen, J. G., Guhathakurta, P., et al. 2013, *ApJ*, 779, 102. doi:10.1088/0004-637X/779/2/102
- Khoperskov, A. V., Khrapov, S. S., & Sirotin, D. S. 2023, *Galaxies*, 12, 1. doi:10.3390/galaxies12010001
- Kormendy, J., Fisher, D. B., Cornell, M. E., et al. 2009, *ApJS*, 182, 216. doi:10.1088/0067-0049/182/1/216
- Lewis, A. R., Dolphin, A. E., Dalcanton, J. J., et al. 2015, *ApJ*, 805, 183. doi:10.1088/0004-637X/805/2/183
- McConnachie, A. W., Irwin, M. J., Ibata, R. A., et al. 2009, *Nature*, 461, 66. doi:10.1038/nature08327
- McConnachie, A. W. 2012, *AJ*, 144, 4. doi:10.1088/0004-6256/144/1/4
- McConnachie, A. W., Ibata, R., Martin, N., et al. 2018, *ApJ*, 868, 55. doi:10.3847/1538-4357/aae8e7
- Mieske, S., Infante, L., Hilker, M., et al. 2005, *A&A*, 430, L25. doi:10.1051/0004-6361:200400119
- Monachesi, A., Trager, S. C., Lauer, T. R., et al. 2011, *ApJ*, 727, 55. doi:10.1088/0004-637X/727/1/55
- Monachesi, A., Trager, S. C., Lauer, T. R., et al. 2012, *ApJ*, 745, 97. doi:10.1088/0004-637X/745/1/97
- Newman, J. A., Cooper, M. C., Davis, M., et al. 2013, *ApJS*, 208, 5
- Norris, M. A., Kannappan, S. J., Forbes, D. A., et al. 2014, *MNRAS*, 443, 1151. doi:10.1093/mnras/stu1186
- Pedregosa, F., Varoquaux, G., Gramfort, A., et al. 2011, *Journal of Machine Learning Research*, 12, 2825. doi:10.48550/arXiv.1201.0490
- Peñarrubia, J., Navarro, J. F., & McConnachie, A. W. 2008, *ApJ*, 673, 226. doi:10.1086/523686
- Quirk, A., Guhathakurta, P., Chemin, L., et al. 2019, *ApJ*, 871, 11. doi:10.3847/1538-4357/aaf1ba
- Quirk, A. C. N., Guhathakurta, P., Gilbert, K. M., et al. 2022, *AJ*, 163, 166. doi:10.3847/1538-3881/ac5324
- Robin, A. C., Reylé, C., Derrière, S., et al. 2003, *A&A*, 409, 523. doi:10.1051/0004-6361:20031117
- Rudenko, P., Worthey, G., & Mateo, M. 2009, *AJ*, 138, 1985. doi:10.1088/0004-6256/138/6/1985
- Rose, J. A., Arimoto, N., Caldwell, N., et al. 2005, *AJ*, 129, 712. doi:10.1086/427136
- Rutledge, G. A., Hesser, J. E., & Stetson, P. B. 1997, *PASP*, 109, 907. doi:10.1086/133959
- Salomon, J.-B., Ibata, R., Reylé, C., et al. 2021, *MNRAS*, 507, 2592. doi:10.1093/mnras/stab2253
- Sarajedini, A., Mancone, C. L., Lauer, T. R., et al. 2009, *AJ*, 138, 184. doi:10.1088/0004-6256/138/1/184
- Sarajedini, A., Yang, S.-C., Monachesi, A., et al. 2012, *MNRAS*, 425, 1459. doi:10.1111/j.1365-2966.2012.21609.x

- Savino, A., Weisz, D. R., Skillman, E. D., et al. 2022, *ApJ*, 938, 101. doi:10.3847/1538-4357/ac91cb
- Schiavon, R. P., Caldwell, N., & Rose, J. A. 2004, *AJ*, 127, 1513. doi:10.1086/381950
- Schlafly, E. F. & Finkbeiner, D. P. 2011, *ApJ*, 737, 103. doi:10.1088/0004-637X/737/2/103
- Schlegel, D. J., Finkbeiner, D. P., & Davis, M. 1998, *ApJ*, 500, 525. doi:10.1086/305772
- Simon, J. D., & Geha, M. 2007, *ApJ*, 670, 313
- Sirianni, M., Jee, M. J., Benítez, N., et al. 2005, *PASP*, 117, 1049. doi:10.1086/444553
- Skilling, J.: Nested sampling for general Bayesian computation. *Bayesian Anal.* 1(4), 833–860 (2006). doi:10.1214/06-BA127
- Sohn, S. T., Majewski, S. R., Muñoz, R. R., et al. 2007, *ApJ*, 663, 960. doi:10.1086/518302
- Sohn, S. T., Anderson, J., & van der Marel, R. P. 2012, *ApJ*, 753, 7. doi:10.1088/0004-637X/753/1/7
- Smith Castelli, A. V., Faifer, F. R., Richtler, T., et al. 2008, *MNRAS*, 391, 685. doi:10.1111/j.1365-2966.2008.13866.x
- Speagle, J. S. 2020, *MNRAS*, 493, 3132. doi:10.5281/zenodo.8408702
- Tang, J., Bressan, A., Rosenfield, P., et al. 2014, *MNRAS*, 445, 4287. doi:10.1093/mnras/stu2029
- Tollerud, E. J., Beaton, R. L., Geha, M. C., et al. 2012, *ApJ*, 752, 45. doi:10.1088/0004-637X/752/1/45
- Paudel, S., Lisker, T., Hansson, K. S. A., et al. 2014, *MNRAS*, 443, 446. doi:10.1093/mnras/stu1171
- Price, J., Phillipps, S., Huxor, A., et al. 2009, *MNRAS*, 397, 1816. doi:10.1111/j.1365-2966.2009.15122.x
- van den Bosch, R. C. E. & de Zeeuw, P. T. 2010, *MNRAS*, 401, 1770. doi:10.1111/j.1365-2966.2009.15832.x
- van der Marel, R. P., de Zeeuw, P. T., & Rix, H.-W. 1997, *ApJ*, 488, 119. doi:10.1086/304690
- van der Marel, R. P., Cretton, N., de Zeeuw, P. T., et al. 1998, *ApJ*, 493, 613. doi:10.1086/305147
- van der Marel, R. P. & Guhathakurta, P. 2008, *ApJ*, 678, 187. doi:10.1086/533430
- van der Marel, R. P., Besla, G., Cox, T. J., et al. 2012, *ApJ*, 753, 9. doi:10.1088/0004-637X/753/1/9
- van der Marel, R. P., Fardal, M. A., Sohn, S. T., et al. 2019, *ApJ*, 872, 24. doi:10.3847/1538-4357/ab001b
- Verolme, E. K., Cappellari, M., Copin, Y., et al. 2002, *MNRAS*, 335, 517. doi:10.1046/j.1365-8711.2002.05664.x
- Walker, M. G., Mateo, M., Olszewski, E. W., et al. 2016, *ApJ*, 819, 53. doi:10.3847/0004-637X/819/1/53
- Williams, B. F., Lang, D., Dalcanton, J. J., et al. 2014, *ApJS*, 215, 9. doi:10.1088/0067-0049/215/1/9
- Williams, B. F., Dalcanton, J. J., Dolphin, A. E., et al. 2015, *ApJ*, 806, 48. doi:10.1088/0004-637X/806/1/48
- Williams, B. F., Dolphin, A. E., Dalcanton, J. J., et al. 2017, *ApJ*, 846, 145. doi:10.3847/1538-4357/aa862a
- Williams, B. F., Durbin, M. J., Dalcanton, J. J., et al. 2021, *ApJS*, 253, 53. doi:10.3847/1538-4365/abdf4e
- Wojno, J. L., Gilbert, K. M., Kirby, E. N., et al. 2023, *ApJ*, 951, 12. doi:10.3847/1538-4357/acd5d3